

The mechanics of adhesion polymers and their role in bacterial attachment

Johan Zakrisson



**Department of physics
Umeå University
2015**

ISBN: 978-91-7601-331-1

Elektronisk version tillgänglig på <http://umu.diva-portal.org/>

Tryck/Printed by: Servicecenter KBC

Umeå, Sweden 2015

Learn from yesterday, live for today, hope for tomorrow
The important thing is not to stop questioning
Albert Einstein

Table of Contents

Appended publications.....	i
Abstract	ii
Sammanfattning	iv
1 Introduction.....	1
1.1 Bacterial adhesion and bio-polymers	1
1.2 Optical trapping and force spectroscopy	2
1.3 Specific aims of this thesis	3
2 Optical tweezers	4
2.1 Optical forces in the trap	4
2.2 Construction	6
2.2.1 Bastun	6
2.2.2 Museum	8
2.2.3 Position detection.....	10
2.2.4 Optimized trapping.....	11
2.3 Improvements of the optical tweezers setup	12
2.3.1 Optical system	12
2.3.2 Calibration techniques.....	14
2.3.3 Fluorescence imaging	19
2.3.4 Flow chamber	20
3 Bacterial adhesion	22
3.1 Environmental conditions	22
3.2 Pili structure and mechanics	23
3.2.1 Investigation of pili mechanics using OT	23
3.2.2 Theoretical description of uncoiling of a helix-like pili.....	26
3.2.3 Investigation of CS2 mechanics	27

3.2.4	Simulations – Rigid body model	29
3.2.5	Simulations – Pili as a shock absorber, a 1D model.....	30
3.2.6	Simulations – Pili as a shock absorber, a 2D model.....	32
3.3	Modeling the adhesin.....	34
3.3.1	Catch-bond mechanics	35
3.3.2	Simulations – survival probability.....	36
3.4	Corrections to Stokes’ drag force	37
3.4.1	Stoke drag force – Near surface correction.....	39
3.4.2	Added mass	40
3.4.3	Basset force	40
3.4.4	Lift force.....	41
3.4.5	Buoyancy	41
3.4.6	Results and conclusions.....	41
4	Method to detect expression of surface organelles	43
5	Digital Holographic Microscopy.....	46
6	Summary of appended papers and my contributions.....	51
7	Acknowledgements	55
8	References	56

Appended publications

- I. N. Mortezaei, B. Singh, **J. Zakrisson**, E. Bullitt, M. Andersson “*Biomechanical and structural Features of CS2 Fimbriae of Enterotoxigenic Escherichia coli*” Biophysical Journal 109 (2015) 49-56.
- II. **J. Zakrisson**, K. Wiklund, M. Servin, O. Axner, C. Lacoursière, M Andersson “*Rigid multibody simulation of a helix-like structure: the dynamics of bacterial adhesion pili*” European Biophysics Journal 44 (2015) 291-300.
- III. **J. Zakrisson**, K. Wiklund, O. Axner, M Andersson “*Helix-like biopolymers can act as dampers of force for bacteria in flows*” European Biophysics Journal 41 (2012) 551-60.
- IV. **J. Zakrisson**, K. Wiklund, O. Axner, M Andersson “*The shaft of the Type 1 Fimbriae Regulates an External Force to Match the FimH Catch bond*” Biophysical Journal 104 (2013) 2137-2148.
- V. **J. Zakrisson**, K. Wiklund, O. Axner, M Andersson “*Investigation of force approximations in tethered cells simulations*” Physical biology 12 (2015) 056006.
- VI. **J. Zakrisson**, B. Singh, P. Svenmarker, K. Wiklund, S. Hakobyan, M. Ramstedt, M. Andersson “*Detecting the presence of surface organelles at the single cell level, a novel cell sorting approach*” Submitted (2015)
- VII. **J. Zakrisson**, S. Schedin, M Andersson “*Cell shape identification using digital holographic microscopy*” Applied Optics 54 (2015) 7442-7448

Abstract

Bacterial resistance to antibiotics is increasing at a high rate in both developing and developed countries. To circumvent the problem of drug-resistant bacterial pathogens, we need to develop new effective methods, substances, and materials that can disarm and prevent them from causing infections. However, to do this we first need to find new possible targets in bacteria to approach and novel strategies to apply.

Escherichia coli (*E. coli*) bacteria is a normal member of the intestinal microflora of humans and mammals, but frequently cause diverse intestinal and external diseases by means of virulence factors, which leads to hundreds of million sick people each year with a high mortality rate. An *E. coli* bacterial infection starts with adhesion to a host cell using cell surface expressed adhesion polymers, called adhesion pili. Depending on the local environment different types of pili are expressed by the bacteria. For example, bacteria found in the gastrointestinal tract commonly express different pili in comparison to those found in the urinary tract and respiratory tract. These pili, which are vital for bacterial adhesion, thereby serve as a new possible approach in the fight against bacterial infections by targeting and disabling these structures using novel chemicals. However, in order to develop such chemicals, better understanding of these pili is needed.

Optical tweezers (OT) can measure and apply forces up to a few hundred pN with sub-pN force resolution and have shown to be an excellent tool for investigating mechanical properties of adhesion pili. It has been found that pili expressed by *E. coli* have a unique and complex force-extension response that is assumed to be important for the ability of bacteria to initiate and maintain attachment to the host cells. However, their mechanical functions and the advantage of specific mechanical functions, especially in the initial attachment process, have not yet been fully understood.

In this work, a detailed description of the pili mechanics and their role during cell adhesion is presented. By using results from optical tweezers force spectroscopy experiments in combination with physical modeling and numerical simulations, we investigated how pili can act as “shock absorbers” through uncoiling and thereby lower the fluid force acting on a bacterium. Our result demonstrate that the dynamic uncoiling capability of the helical part of the adhesion pili modulate the force to fit the optimal lifetime of its adhesin (the protein that binds to the receptor on the host cell), ensuring a high survival probability of the bond.

Since the attachment process is in proximity of a surface we also investigated the influence of tether properties and the importance of different surface corrections and additional force components to the Stokes drag force during simulations. The investigation showed that the surface corrections to the Stokes drag force and the Basset force cannot be neglected when simulating survival probability of a bond, since that can overestimate the probability by more than an order of magnitude.

Finally, a theoretical and experimental framework for two separate methods was developed. The first method can detect the presence of pili on single cells using optical tweezers. We verified the method using silica microspheres coated with a polymer brush and *E. coli* bacteria expressing; no pili, P pili, and type 1 pili, respectively. The second method was based on digital holography microscopy. Using the diffraction of semi-transparent object such as red blood cells, we showed that this method can reconstruct the axial position and detect morphological changes of cells.

Sammanfattning

Bakteriell resistens mot antibiotika ökar i hög takt i både utvecklingsländer och industriländer. För att kringgå problemet med läkemedelsresistenta bakteriella patogener, måste vi utveckla nya effektiva metoder, ämnen, och material som kan hindra dem från att orsaka infektioner. För att göra detta måste vi först hitta nya möjliga mål och strategier för att angripa dessa bakterier.

Escherichia coli (*E. coli*) bakterier är en normal medlem i tarmfloran hos människor och däggdjur, men orsakar även infektioner genom virulensfaktorer, vilket leder till hundratals miljoner sjuka människor varje år med hög dödlighet. En *E. coli*-bakteriell infektion börjar med att bakterierna måste vidhäfta till en värdcell via de vidhäftningspolymerer som uttrycks på cellytan, som kallas pili. Beroende på de lokala miljöerna kan olika typer av pili uttrycks av bakterierna. Till exempel, bakterier som finns i mag-tarmkanalen uttrycker vanligtvis andra typer av pili i jämförelse med de som finns i urinvägar och andningsorgan. Dessa pili, som är avgörande för bakteriell vidhäftning kan därmed fungera som en ny möjlig strategi i kampen mot bakteriella infektioner genom att inaktivera dessa strukturer med hjälp av nya kemikalier. Men för att utveckla sådana kemikalier behövs bättre förståelse av dessa pili.

Optiska pincetter (OT) kan mäta och applicera krafter upp till några hundra pN med sub-pN kraft-upplösning, och har visat sig vara ett utmärkt verktyg för att undersöka mekaniska egenskaper hos pili. Det har visat sig att pili uttryckt av *E. coli* har en unik och komplex kraft-förlängningsrespons som antas vara viktiga för förmågan hos bakterierna att initiera och upprätthålla vidhäftning till värdcellerna. Dock har deras mekaniska funktioner och fördelen med dessa mekaniska funktioner, särskilt i den inledande vidhäftningsprocessen, ännu helt inte klarlagts.

I detta arbete presenteras en detaljerad beskrivning av de mekaniska egenskaperna hos dessa pili och deras roll i den initiala adhesionsprocessen. Genom att använda resultat från kraftspektroskopi-experiment i kombination med fysikalisk modellering och numeriska simuleringar, undersökte vi hur pili kan fungera som "stötdämpare" genom förlängning av dess helix-lika struktur och därigenom sänka vätskekrafterna som verkar på bakterien. Vårt resultat visar att den dynamiska förlängningen av dess helix-struktur kan modulera den externa kraften för att passa den optimala livslängden för dess adhesin (det protein som binder till receptorn på värdcellen), vilket garanterar en hög överlevnadssannolikhet av bindningen.

Eftersom fästprocessen är i närheten av en yta, undersöktes även inverkan av olika ytkorrigeringar och ytterligare kraftkomponenter till Stokes dragkraft

genom olika simuleringar. Resultaten visade att ytkorrectionerna till Stokes dragkraft och Basset-kraften inte kan försummas vid simulering av överlevnads-sannolikheten för en bindning, eftersom det kan överskatta sannolikheten med mer än en storleksordning.

Slutligen har ett teoretiskt och experimentellt ramverk för två separata metoder utvecklas. Den första metoden kan detektera närvaron av pili på enskilda celler med användning av den optiska pincetten. Vi verifierade metoden med mikrostora glaskulor belagda med en polymer på ytan och *E. coli*-bakterier som uttrycker; ingen pili, P pili, och typ 1 pili, respektive. Den andra metoden bygger på digital holografisk mikroskopi. Från diffraktionsmönstret av semitransparenta föremål såsom röda blodkroppar, visade vi att denna metod kan rekonstruera den axiella positionen och detektera morfologiska förändringar hos celler.

1 Introduction

1.1 Bacterial adhesion and bio-polymers

Pathogenic bacteria such as uropathogenic *Escherichia coli* (UPEC) and enterotoxigenic *Escherichia coli* (ETEC) infect millions of people every year, many with deadly outcome. ETEC is one of the main causes of travelers' diarrhea in developing countries [1, 2], causing an estimated 300 000 – 500 000 deaths every year [3]. UPEC is the most common cause of urinary tract infection (UTI), and 25-30% of the women that previously had an UTI will suffer from recurrent UTIs [4, 5]. Unfortunately, the intense use of antibiotics has promoted bacteria to develop antibiotic resistance due to mutation [6]. This has led to an urgent need to find new methods for battling bacterial infection like UTI.

The initial step of a bacterial infection starts with bacteria attaching to host cells. Since both bacteria and host cells are negatively charged, and thereby will repel each other, bacteria have developed different types of surface organelles to overcome this issue [7]. Thus, these surface organelles are a key part of the infectious ability of bacteria [8], and it has been shown that these adhesive surface organelles, known as fimbriae or pili [9], are in many cases vital for the initial colonization of bacteria. In addition, they can help bacteria to stay attached to host cells during fluid flow preventing the bacteria to be flushed out [10]. This means that the pili mediating the attachment of the bacteria to the host cell can be an alternative angle of attack of battling bacterial infections. To do this, the mechanical function of these complex bio-polymers and their adhesin need to be understood.

Previous data shows that several classes of pili expressed by ETEC and UPEC are assembled from a large number of identical sub-units $\sim 10^3$ that are helically organized with ~ 3 sub-units per turn, which creates a structure that is ~ 7 -10 nm wide and ~ 1 -2 μm long [11–15]. This particular helix-like structure can be uncoiled under a mechanical load. The response of the pili from a mechanical load is what makes the pili so vital in the adhesion process. It can, by partially uncoil itself, reduce and redistribute the load from the shear force as shown in rolling experiments [16, 17]. It is thereby hypothesized that its flexibility and ability to uncoiling enable the bacterium to withstand the shear forces during fluid flows [14, 18]. Therefore, it is of great importance to learn more about the mechanical function of these pili.

1.2 Optical trapping and force spectroscopy

The fundamentals of optical trapping was developed by Arthur Ashkin during the seventies [19–21]. Even though he demonstrated that small particles such as dielectric spheres (1-100 μm in diameter) could be manipulated by optical forces, it took until 1986 before the single beam optical trap was demonstrated [22]. The single beam optical trap creates a 3D-potential pulling the trapped object towards the center of the laser focus. Shortly after this break-through, Ashkin showed that objects like viruses and bacteria also could be trapped [23] showing the vast potential of optical tweezers in biology.

An important application of the single beam gradient trap is the force measuring optical tweezers (FMOT). Since the trap acts like a harmonic potential, a displaced object in the trap relative to the center of the trap will experience a restoring force. This restoring force can be described by means of Hooks law. Using this technique, positions and forces can be measured at sub-nm and sub-pN resolution [24–26]. Such a high resolution cannot be achieved by atomic force microscopy (AFM), which is a common technique used to measure forces in biological systems. In addition, Optical tweezers is a non-invasive tool using exclusively light, meaning it is sterile [27, 28]. Even though it is a non-invasive method, it can still cause damage to the sample, e.g., a cell. To maintain the viability of a trapped cell, care must always be taken to avoid a high absorption of the laser light, which can damage the cell as reported in several studies [29–32].

The trap itself is usually formed using a high numerical aperture (NA) microscope objective and the setup is usually built around an inverted microscope [33, 34]. This makes imaging of the sample easy since all optics is already there. In addition, it also makes it very straight forward to include more features like fluorescence imaging and flow chambers. The trapped object, if it is non-spherical, it will self-orient in the trap implying that its orientation will be known even if it is not seen in the microscope. All this is a big advantage compared to other manipulation techniques, such as AFM.

Optical tweezers (OT) has grown to be an important tool with many applications within physics, biology, material science, and chemistry. In particular, within the field of biology, OT has proven useful for cell sorting and organization, precise manipulation of microstructures, alterations of polymer structures (e.g., uncoiling and characterizing of proteins) characterization of molecular motors, or for investigating interactions

between, e.g., red blood cells and viruses, and binding forces [35–38]. Torque on non-spherical objects can also be measured, which is useful when investigating for example the mechanical properties of the DNA structure [36, 39].

1.3 Specific aims of this thesis

The main work in this thesis was aimed at investigating the initial adhesion process of pathogenic bacteria as well as elucidating how pathogenic bacteria can attach and remain attached in *in vivo* fluidic environments, from a physicist point of view.

Pathogenic bacteria, like UPEC, attach themselves with certain surface organelles, i.e., pili. In our lab, we investigate the mechanics of pili by performing force spectroscopic measurements using optical tweezers. Thereby, a part of my work was dedicated to a continued development and improvement the OT setups. This included updating optical components to optimize the trapping, introducing new optics to combine the optical trapping with fluorescence and flow chambers, as well as reducing the noise to improve on the signal-to-noise ratio. In addition to the instrumental work, I have continuously worked with updating and adding new routines to the tailor made control program needed to control the OT setups.

The major part of my work was focused on investigating the mechanics of the pili and how their specific mechanical properties are utilized in the adhesion process in a high shear fluid flow environment. Since these systems easily become very complex, computer models recreating the pili mechanics and its surrounding fluid environment, with a main focus on the UPEC bacteria, was developed. Using these models in combination with experimental data, we can get a better understanding of how the adhesion process is mediated. In addition, we investigate which of the mechanical properties of the pili and adhesin that is vital in the initial attachment and colonization process.

2 Optical tweezers

The concept of radiation pressure was founded 1619 by Johannes Kepler to describe why the comet tail always is directed away from the sun. The radiation pressure that is pushing the tail away from the sun comes from a change of momentum of the photons. This change in momentum of a single photon is very small, but in large numbers and for small objects, this effect becomes significant. Any change of direction of the photon will change the momentum, giving rise to a force acting upon the object. This force can be divided into two components, the scattering and the gradient force. By strongly focusing a laser beam using a high NA objective, the arising gradient force will push the object towards the center of the focus, while the scattering force will push it in the direction of the light. The object will be trapped in an OT where the gradient and scattering force balance each other.

Optical tweezers are thus an instrument that allows trapping of micrometer sized particles with the exclusive use of laser light. By either moving the focus of the laser beam, or the sample, the OT will give unsurpassed possibilities to manipulate the position of the particle. The technique works on both “inert” particles (for example silica, polystyrene, latex, or gold beads) and “living” biological objects (single cells, including bacteria).

By also monitoring the deflection of the laser light from a trapped spherical particle, using a photo-sensitive detector in the setup, it is possible to measure minute forces, as is done in force measuring optical tweezers (FMOT). This is possible since the light field creates a harmonic potential for the trapped object, which in turn implies a linearly increasing force for displacement of the trapped object relative the center. By knowing the trap stiffness and measuring the position of the object in the trap, the force that acts upon an object can thereby be accurately determined.

2.1 *Optical forces in the trap*

Optical forces can be explained using a variety of theories that often are expressed in terms of the ratio between the size of the object and the wavelength of the light. Commonly, two regimes are considered; for particles much smaller than the wavelength of the light the dipole approximation should be considered [22], whereas for particles significantly larger than the wavelength of the light, the ray optics approximation can be used. When the particles are roughly the same size as the wavelength, a complete model of

the light-particle interaction must be used to calculate the optical forces.

In the Rayleigh regime, the object can be seen as a dielectric dipole interacting with an electromagnetic field [40]. If there is a gradient in the electromagnetic field, a force proportional to the gradient will act onto the object in the direction of the gradient. For example, if a Gaussian beam is focused, the gradient will always point towards the focus of the laser beam, thus creating a 3D potential, which will allow trapping of an object.

In the ray optics regime, in which the particle is assumed to be much larger than the wavelength of the incident light [41], the object is seen as a geometrical object reflecting or refracting the light. By using the fact that each photon (ray) carries a momentum, which will be changed when it is reflected or refracted, a force will act upon the object. The net force can thus be calculated by summing the contribution from all rays.

Trapping in the lateral plane, i.e., perpendicular to the light propagation, is possible if the beam has a symmetric intensity gradient, such as a Gaussian laser beam that is illustrated in Figure 1A. However, due to the scattering of the photons when interacting with a material of different index of refraction the object will be pushed in the direction of the light. To circumvent this

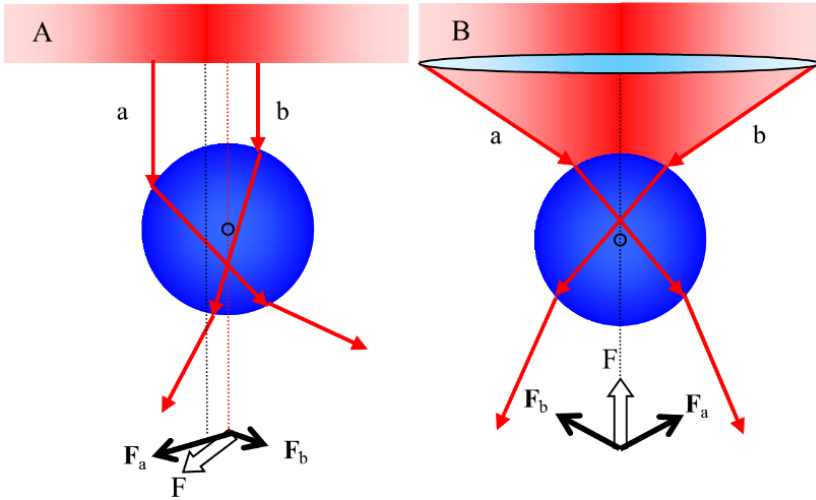


Figure 1. Illustration of the total restoring force, F , acting on a slightly displaced trapped sphere in the ray optics regime. A) Two rays with the same intensity, a and b , is refracted through a displaced bead. Since ray a will be refracted stronger than b , the resulting force will be directed to the left. B) Using a high NA objective, a gradient along the optical axis is also formed, creating a restoring force towards the center of the focus.

problem and allow axial trapping, Ashkin successfully introduced a counteracting laser beam [19, 20]. Later, Ashkin showed that by using a high NA objective it is possible to allow for trapping in 3D using a single laser beam, thus the single beam optical trap was founded [41], as shown in Figure 1B.

2.2 Construction

The two OT setups in the Biophysics and Biophotonics group at Umeå University, called the “Bastun” (eng. the sauna) and the “Museum”, are located in separate temperature and humidity controlled rooms so thermal drifts of the mechanics can be reduced. Each setup is placed on a floating optical table that reduces vibrations from the ground. Major heat and noise sources, such as computers and the power supply to the laser, are located in a separate air-conditioned room to further reduce noise and minimize temperature fluctuations.

2.2.1 Bastun

As is shown in Figure 2, the “Bastun” setup is constructed around an inverted microscope (IX-71, Olympus) that has been modified with the additional components needed for optical trapping and force spectroscopy measurements. Figure 3 provides an illustration of the microscope and its components. The trapping laser (Nd:YVO₄ operating at 1064 nm) is located behind the microscope and covered with black hardboard (TB4, Thorlabs) to isolate the laser beam and reduce fluctuations that otherwise can be influenced by air moving in the room. Before the trapping laser beam enters the microscope on the right side, the beam is shaped using optical components for controlling the position of the trap in the sample chamber and to overfill the back aperture of the objective to a suitable amount. These components are listed and described in detail in section 2.3.1. The probe laser, which is used to monitor the position of the trapped object, is a red fiber-coupled He-Ne laser (operating at 632.8 nm). An output coupler focuses the probe laser light before it enters the microscope from the left. Inside the microscope the two lasers are combined using a polarizing beam splitter cube (PBSC), where after the beams reach the microscope objective (UplanFl 100x/1.3 Oil, Olympus). The sample is placed above the microscope objective on a piezoelectric stage (E517 controller with a P-561.3CD stage, Physik Instrument), which controls the axial and lateral position of the sample with sub-nm resolution. The piezo-stage is, in turn, mounted on a joy-

stick controlled step-motor table so the operator can manually control the position of the sample. For coarse control of the sample the joy-stick is used and for fine movements and force spectroscopy measurements the piezo-stage is used, respectively. In Figure 3 a schematic illustration of the components in the setup is shown.

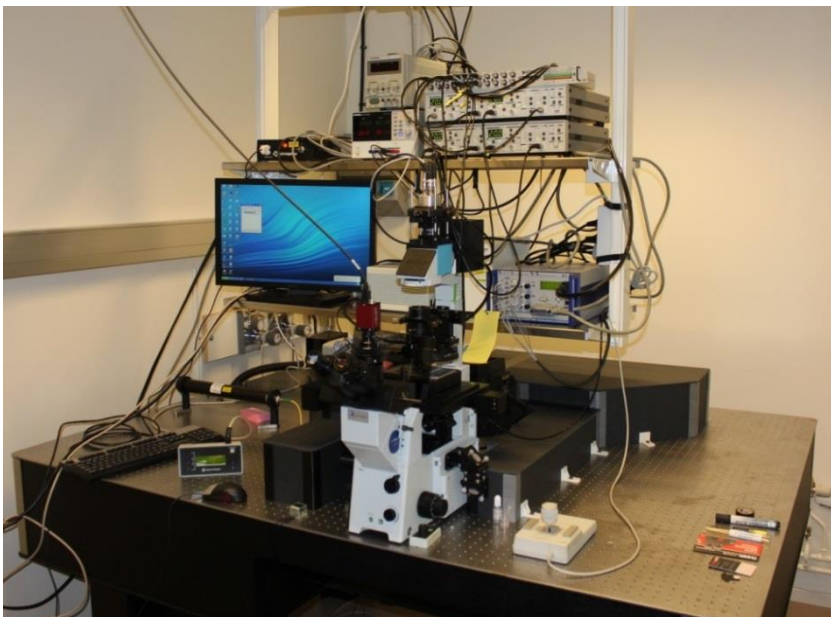


Figure 2. A picture of the “Bastun” optical tweezers setup. The trap laser is behind the microscope and the entire path of the laser beam, from the laser to the objective, including optics, are covered (the black box-like structure on the right). Similarly, the probe laser is also covered (box on the left side of the microscope). The computer screen displays the video feed of the sample.

An object that is trapped is illuminated by the probe laser beam, which is collected by the microscope condenser that directs the laser light to a position sensitive detector (PSD) to monitor the position of the object in the trap. The signal from the PSD is sent to two combined low-pass filters with an integrated amplifier (SR640, Stanford research systems) before it is sent to an A/D-card (PCI 6259M, National Instruments) in the computer. The data are then processed in an in-house LabVIEW program. The scattered light from the sample and object is collected by the microscope objective and sent to the eye-piece and the camera (DX 2 HC-VF, Kappa, alternatively a Stingray F125C, AVT). Before the light enters the eye-piece and the camera, a laser-

line (LL) filter removes the light from the trapping laser, and an additional filter prevents the light from the probe laser to enter the camera. The camera and the eye-piece are used for orientation in the sample chamber when using the joy-stick and for visual support during experiments.

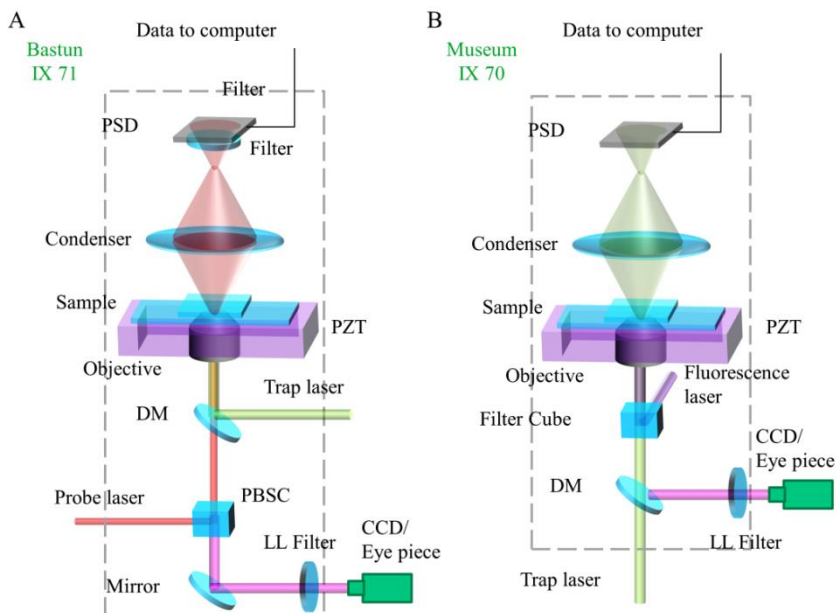


Figure 3. A) Illustration of the “Bastun” microscope and its components, represented by the grey dashed line. The probe laser enters from the left, and is merged with the trap laser using a dichroic mirror (DM). The two lasers then enter the objective, where the trap laser forms the trap. The laser light is collected by the condenser which sends the light to the PSD. A filter prevents the trap laser light reaching the PSD. The light from the illumination of the sample is collected by the objective and sent to the eye-piece and camera. An LL-filter prevents any light from the trap laser reaching the eye piece. B) Illustration of the “Museum” microscope and its components. Here the trap laser enters from below and is merged with the fluorescence laser in the filter cube. This setup uses the trap laser for position detection as well, i.e., there is no probe laser.

2.2.2 Museum

The “Museum” setup is constructed around an inverted microscope (IX-70, Olympus). The trapping laser (Rumba 2000, 1024 nm, Cobolt) is located below the microscope and the beam is sent from underneath into the microscope. Figure 4 shows a picture of the Museum setup and Figure 3B

shows an illustration of the microscope and the beam paths.

In this setup, no additional laser is used for probing the position of the trapped object. Therefore, no laser-line filter is positioned in front of the PSD. The laser is introduced from underneath the microscope and passes the filter cube before entering the water immersion microscope objective (UPlanSApo 60x water, Olympus). The piezoelectric stage (E725 controller with a P-561.3CD stage, Physik Instrument) controls the axial and lateral position of the sample during measurements. The piezo stage is, in turn, mounted on a joy-stick controlled step-motor table which is used for lateral orientation in the sample. Here a high-speed camera (C11440-10C, Hamamatsu) is used for imaging of the sample; again, an LL-filter prevents the laser light reaching the camera and eye-piece.

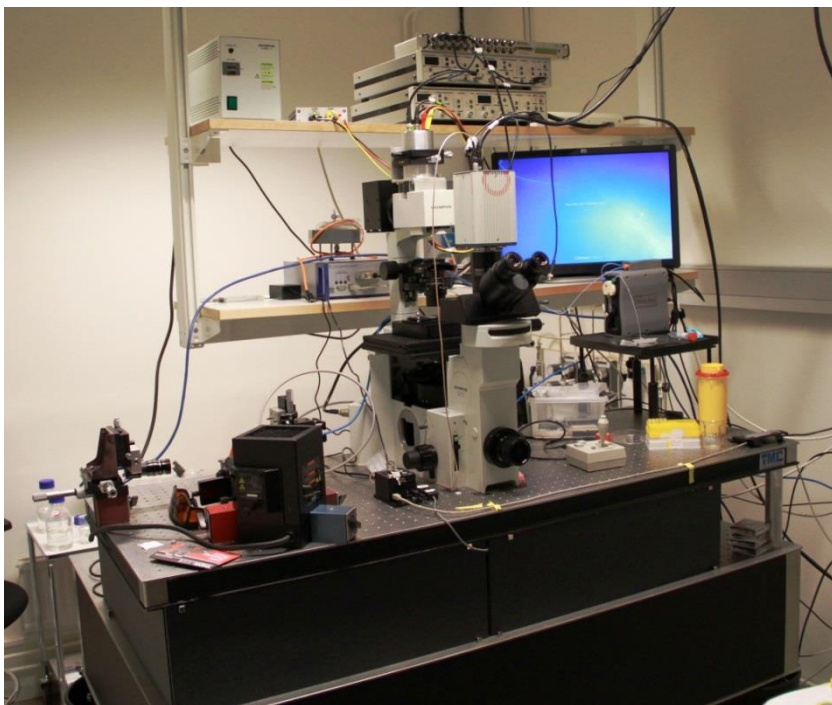


Figure 4. A picture of the “Museum” optical tweezers setup. The trap laser is underneath the microscope and the entire path of the laser light from the laser to the objective is covered (between the two table tops). The computer screen displays the video feed of the sample. Just below the display is the pump for the flow chamber system.

This setup has also been integrated with a blue laser (Calypso 50, 491 nm, Cobolt), introduced into the microscope via the back port, to allow for fluorescent imaging. Combined trapping and fluorescent imaging is made possible by a special fluorescence filter cube positioned in the microscope. This is further explained in section 2.3.3.

In addition, a flow chamber system has been integrated into the setup, which is further described in section 2.3.4. The flow chamber enables more elaborate experiments emulating more realistic conditions when studying cell rolling etc. The system is designed so flow chamber experiments, in combination with fluorescence and optical trapping, can be performed simultaneously.

2.2.3 Position detection

Accurately determining the position of the trapped object, e.g., a spherical micro-particle, is vital when measuring forces using OT. The force measurements are possible since the trapped object will act as it is residing in a harmonic potential, thus there is a linear relation for relative displacements in the trap. An illuminated trapped object creates an interference pattern by refraction and scattering of the probe laser beam, which is collected by the condenser and directed to the PSD. The interference pattern on the PSD from the trapped sphere is centered with symmetric intensity when the system is calibrated and the trapped sphere is in the center of the trap. If the sphere moves, the interference pattern will change its intensity distribution on the PSD giving rise to a change in the output signal of the PSD. The PSD in turn converts the incoming light to four continuous photocurrents, two for each lateral direction (x_- , x_+ , y_- , and y_+) that are converted to a voltage signal. Figure 5 shows a picture of the PSD and its four lateral signals. If the laser hits the center of the PSD, all signals from the four channels are equal. When the object in the trap moves, the intensity of interference pattern on the PSD will change correspondingly. For example, if the object is moved to the right in the sample (positive x -direction), the signal in x_+ will be linearly stronger relative to the movement of the object, while it becomes equally weaker in the x_- direction. The four signals can be normalized in respective lateral direction (to have a signal from -1 to 1) by setting $X = (x_+ - x_-)/(x_+ + x_-)$ and $Y = (y_+ - y_-)/(y_+ + y_-)$, where X and Y are the normalized position in x - and y -direction of the incident light on the PSD. This signal is then multiplied with a conversion factor to find the absolute displacement or relative movement of the trapped particle. This is discussed in section 2.3.2.

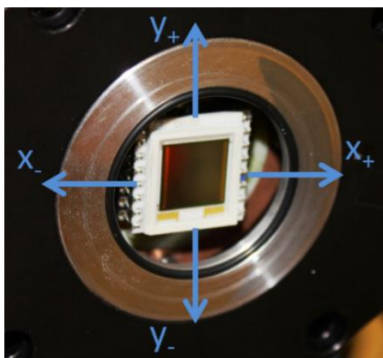


Figure 5. A picture of the 2D PSD with its four lateral signals x_- , x_+ , y_- , and y_+ .

2.2.4 Optimized trapping

It is desirable to achieve an efficient trap, i.e., using as low laser power as possible but still achieve a strong trap, for several reasons. High intensity of the trapping laser can damage the optics, including the microscope objective, which usually are made to transmit visible light with high transmission [42]. High laser power will also locally heat the sample, usually a few K/W. This will change the viscosity of the sample and influences the trap stiffness [43, 44]. In addition, photo damage to biological samples can occur at high intensities [23, 30]. Therefore, the optimum solution is to have a well-shaped trap that will generate as strong trap as possible with the lowest laser power possible. A well-shaped trap is achieved by minimizing the optical aberrations in the system. How this is done is discussed in detail in section 2.3.1.

The trap strength will also increase with increasing index of refraction of the trapped object relative to the surrounding media. In general it is not possible to change this since biological samples often require a certain solution to ensure the cells mechanical functions are reliable.

As discussed above, the axial trapping is dependent on the axial gradient, which is a function of the NA of the objective. Therefore, strong axial trapping is realized for a $NA \geq 1.2$ (i.e., a higher NA implies larger axial gradient). Moreover, when using a laser beam with a Gaussian shape mode (TEM_{00}), the weakest rays (i.e., the outermost rays) will be the rays with the highest incident angle to the object. Therefore, the laser beam should be slightly larger than the entrance aperture, i.e., overfilling the objective to optimize the axial trapping since it is the outer most rays in the objective that has the largest effect on the axial trapping. Typically, 80-90% of the intensity

of the laser beam should enter the objective to achieve good axial trapping [44].

2.3 Improvements of the optical tweezers setup

Continuously improving the OT technique is important since it is the development of new measurement techniques that allow new and better experiments leading to novel discoveries. Consequently, improving and updating the OT setups have been a part of my work in the group. In this chapter, I describe the parts of what I have developed or taken part of.

2.3.1 Optical system

The optical system that introduces the laser light into the microscope controls both the position of the optical trap along the optical axis and the degree of overfilling of the entrance aperture of the objective. This system was optimized in mainly two ways; by reducing vibrations in the optical system and reducing the optical aberrations. A system with less vibration will be more stable and thereby making the data more reliable. In addition, less aberration in the system will give the trap a better shape making it possible to trap using objects lower laser power, as well as allow for trapping of smaller particles and extend the trapping range to also trap significantly higher up from the surface.

To improve the optical system I first simulated the beam path, i.e., the optical system, using Zemax simulation software. From the simulation the optimal components for the system were identified. A so called cage system was introduced and the old lenses were replaced with the lenses that minimized the optical aberrations in the system. A cage system consists of four rods that go through each corner of the optical mounts, making alignment of the mounts and the optics easy, see Figure 6. Since this system is significantly easier to align, aberrations from misalignment of system can be significantly reduced. The cage system is also very rigid and sits close to the optical table thereby minimizing vibrations in the optical mounts.

Except for the microscope objective, the lenses presented in Figure 6 are the only three lenses in the whole path between the laser and the trap in the new system. Together, these three lenses constitute a so called Cooke triplet, which is a set of three lenses; a positive, a negative, and a positive. This type of lens system is commonly used as a simple and effective way of constructing a camera objective. Similar to a camera objective, the Cooke triplet was designed to work as an adjustable beam expander (zoom) with the

possibility to also adjust the divergence (focus). The Cooke triplet used in the OT setup is constructed by; L1 (LA1331, $f = 60$ mm, Thorlabs), L2 (LD2060, $f = -15$ mm, Thorlabs), and L3 (LA1461, $f = 250$ mm, Thorlabs).

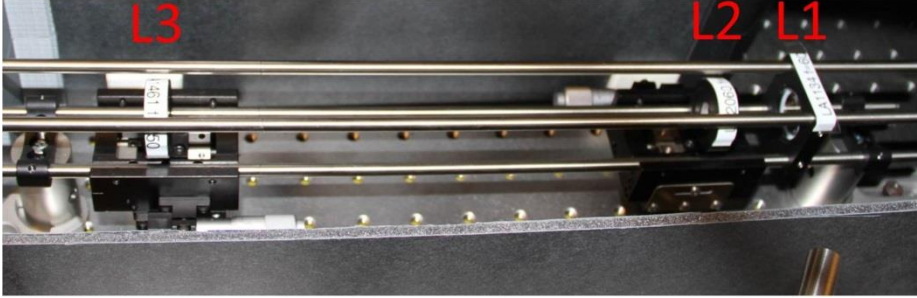


Figure 6. A picture of the beam expander built using a cage system. Lenses L1, L2, and L3 are the three lenses used as a beam expander and to adjust the divergence of the laser beam. The divergence of the laser beam controls the axial position of the trap.

In a regular inverted microscope a tube lens is mounted to form an infinity-corrected system. Since the laser light needs to be parallel into the objective, with this in place, another lens is needed to make the system afocal. In the old setup, these two lenses, in combination with a gimbal mounted mirror (GMM) positioned in the image plane of the entrance aperture of the objective, controlled the lateral position of the optical trap during the calibration of the optical trap. An illustration of how the lateral position of the trap was controlled is shown in Figure 7.

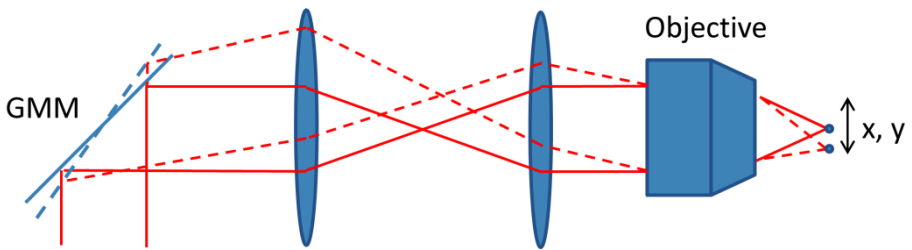


Figure 7. An illustration of how the movement of the trap in the lateral plane can be achieved by tilting a GMM. The GMM is placed in the image plane of the entrance aperture of the objective ensuring that the intensity entering the objective is unaltered when tilting the GMM.

In the present setup, a piezoelectric stage is used to move the sample chamber, instead of moving the trap and thereby the object, during the

calibration procedure, meaning that these two lenses could be removed and the GMM was replaced with a regular mirror. This reduced the optical aberrations in system. In addition, the additional step to convert the pivot angle to lateral movement is not needed, making the new calibration procedure faster and easier to use. Care should however be taken when oscillating the sample since acceleration of the sample might cause fluid flows that affects the calibration constant. To avoid this problem we use small sealed chambers and low accelerations.

To control the trap along the optical axis, two additional lenses were used in the old setup. These two lenses were in conjugate with the back entrance aperture of the objective. By moving one of these lenses, the trap could be moved up or down without changing the overfilling of the objective. These lenses were also removed in favor of the Cooke triplet since the new system also controls the divergence of the laser.

Also, the dichroic mirror in the “Bastun” (noted DM in the “Bastun” in Figure 3A) was replaced with a PBSC (PBS252, Thorlabs). The DM had quite poor surface quality (we assume the mount bended the mirror), and by changing the DM to a PBSC that is much more rigid, the quality of the laser beam was improved allowing for strong trapping of 1 μm sized polystyrene beads.

2.3.2 Calibration techniques

The calibration of the optical trap is an important step before performing any force measurements since the accuracy of the calibration dictates the reliability of the succeeding measurements. There are four commonly used methods of calibrating the trap; the Stokes’ method, the equipartition theorem, the passive-, and active power spectrum method. The active power spectrum method is fast and is considered most reliable since it requires no prior knowledge of the temperature of the sample, viscosity, size of the trapped object, and height of the trapped object above the surface [45]. The method also simultaneously measures the conversion factor that converts the positional data from the PSD (given in volt) to μm . The passive power spectrum method that previously was used in the setup requires knowledge of the temperature, viscosity, size of the trapped object, and the height above the surface. Furthermore, it does not simultaneously find the conversion factor for the positional data from the PSD. Below is a theoretical description of all four calibration methods.

The focused laser beam forms a harmonic potential well for spherical

objects. Therefore, the optical trap can for small displacements of a trapped object be described as a Hookean spring, i.e., $F_{Trap} = -\kappa \cdot x$, where κ is the spring constant (the trap stiffness) and x is the elongation of the spring, i.e., the displacement of the trapped object relative the center of the trap.

The Stokes' method is based upon the Stokes drag force, which is the force acting on a microsphere in a flow, and is defined as

$$F_D = 6\pi\eta rv, \quad (1)$$

where η is the dynamic viscosity, r is the radius of the sphere, and v is the velocity of the liquid relative to the sphere. To find the trap stiffness, a bead is trapped and moved relative the surrounding liquid with a given velocity. Note that in general the trap is stationary and the sample moved by a piezo-stage. The position of the object relative the trap, x_d , can be measured using either a camera or the deflected laser beam. The trap stiffness can thereby be calculated as

$$\kappa = \frac{F_D}{x_d}. \quad (2)$$

It is also possible to use the energy of the thermal motion of a small trapped particle, as given by the equipartition theorem. In each degree of freedom the energy is given by

$$E_{th} = \frac{1}{2} k_B T, \quad (3)$$

where k_B is Boltzmann constant and T is the temperature [46]. Then, by using the variance of the thermally induced displacements, the trap stiffness can be derived by

$$\kappa = \frac{k_B T}{\langle [\Delta x(t)]^2 \rangle}, \quad (4)$$

where $\langle [\Delta x(t)]^2 \rangle$ is the mean square displacement of the trapped particle [46].

The passive power spectral density is commonly used for calibration of an optical trap and it can be derived from the Langevin equation using the

motion for a trapped microsphere [42, 46, 47]. The particle movement in the harmonic potential is described by

$$m\ddot{x}(t) + \gamma_0\dot{x}(t) + kx(t) = (2k_B T \gamma_0)^{1/2} \xi(t), \quad (5)$$

where m is the mass of the particle, γ_0 is the viscous drag coefficient (assuming a laminar flow), and $\xi(t)$ is a normally distributed stochastic term, i.e., $\langle \xi(t) \rangle = 0$. Note that the history force mentioned in ref. [46] (and described in section 3.4.3), is omitted in the Langevin equation presented in Eq. (5). Assuming an over damped system, the first term of Eq. (5) can be neglected [48], giving

$$\gamma_0\dot{x}(t) + kx(t) = F(t), \quad (6)$$

where $F(t)$ represents the right hand side term in Eq. (5) and $F(t)$ is the stochastic force with an average value of zero, i.e., $\langle F(t) \rangle = 0$ [49]. The power spectral density can be found using the Fourier transform of $F(t)$, which for Brownian motion is $S_F(f) = |F(f)|^2 = 4\gamma_0 k_B T$. The power spectral density of the motion of the particle can thus be written as

$$S_x(f) = \frac{k_B T}{\gamma_0 \pi^2 (f^2 + f_c^2)} = \frac{D}{\pi^2 (f^2 + f_c^2)}, \quad (7)$$

where f_c is the corner frequency separating the unsuppressed Brownian motion and the suppressed Brownian motion due to the optical trap and D is the diffusion coefficient (given by the Stokes-Einstein equation). The trap stiffness is related to the corner frequency and drag coefficient, and is given by

$$\kappa = 2\pi\gamma_0 f_c. \quad (8)$$

Since the PSD gives the position in volt, a conversion factor, β , is needed to convert the position from volt to meters. There are two methods of finding this factor in the passive power spectral method. The first method, described below, is based on moving a trapped bead through the probe laser beam while recording the position data. This approach was previously used. The second method is based on the theoretical expression of Stokes drag coefficient, and do not require any movement of the trap.

In old method the conversion factor was found by moving a trapped bead through the beam from the probe laser using a GMM. By combining the positional data and the signal from the PSD, a signal-vs.-displacement curve can be assessed, as schematically illustrated in Figure 8. The signal from the PSD has one maximum and one minimum, and it is the slope of the linear region between these two peaks (red dashed curve) that gives the conversion factor β , which has the unit of $V/\mu m$.

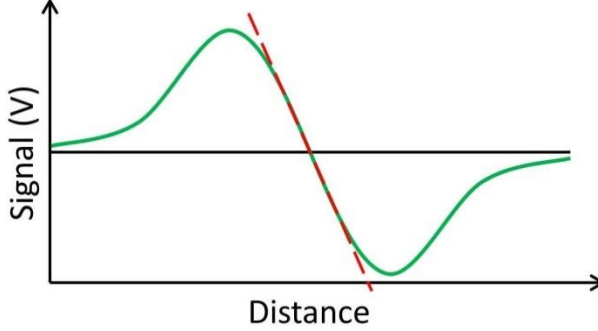


Figure 8 show the typical shape of the response of the detector when the probe laser passes a bead. The slope red dashed curve gives the conversion factor β .

The second method to find the conversion factor is based upon the power spectral density. As previously discussed, the positional data is given in volt, and the power spectral density from the PSD data is thereby given by

$$P(f) = \frac{D^V}{\pi^2 (f^2 + f_c^2)}, \quad (9)$$

where D^V is the diffusion coefficient where the length unit is measured in volt. By comparing Eq. (7) and (9), we can set $D = \beta^2 D^V$, giving

$$\beta = \sqrt{D/D^V} = \sqrt{6\pi\eta r/k_B T D^V}. \quad (10)$$

Note that the friction coefficient in Eq. (8) is given by $\gamma_0 = k_B T/D$. This mean that the trap stiffness can be rewritten to

$$\kappa = 2\pi f_c \frac{k_B T}{D}. \quad (11)$$

The active power spectrum method is very similar to the passive. There is only one significant difference, during the calibration the sample is oscillated, which I call the “oscillation” method (described in detail in ref. [50]). This means that one more term is added to the Langevin equation, and thereby also to Eq. (7) to account for the induced oscillatory movement of the sample. The power spectral density is then modified to

$$P(f) = \frac{D}{\pi^2(f^2 + f_c^2)} + \frac{A^2}{2(1 + f_c^2/f_{drive}^2)} \delta(f - f_{drive}), \quad (12)$$

where A is the amplitude of the oscillation and f_{drive} is the frequency of the oscillation. The power spectral density of the positional data will have a clear peak at the oscillation frequency. Figure 9 presents a power spectrum of a trapped polystyrene bead where the sample is oscillated at 32 Hz with an amplitude of 108 nm. Again, note that the PSD provides the positional data in volt. This means that the diffusion constant in Eq. (12) will be denoted D^V when performing the calibration. By fitting the first term in Eq. (12) to the power spectrum, the corner frequency, f_c , indicated with a green dot in Figure 9, and the diffusion coefficient, D^V , where the amplitude of the power spectral density is given in V^2/Hz , can be determined.

Since the PSD gives the position in volts, a conversion from volt to nm has to be performed. Again, by setting $D = \beta^2 D^V$, except β is in this case given by

$$\beta = \sqrt{W_{th}/W_{ex}}, \quad (13)$$

where W_{th} is the theoretical peak height and W_{ex} is the experimental peak height, and is given by

$$W_{ex} = [P^V(f_{drive}) - P_T^V(f_{drive})] / t_{msr}, \quad (14)$$

where $P^V(f_{drive})$ is the experimental peak height, $P_T^V(f_{drive})$ is the thermal background, which is the plateau at low frequencies in the power spectral density, and t_{msr} is the measurement time for a single power spectrum. The green arrow in Figure 9 indicates how W_{ex} is determined, where the experimental peak height and the thermal background are indicated by green

dots. The theoretical peak height is given by

$$W_{th} = \frac{A^2}{2(1 + f_c^2 / f_{drive}^2)}. \quad (15)$$

Using that the drag coefficient in Eq. (8) can be expressed as $\gamma_0 = k_B T / D$, where $D = \beta^2 D^V$, the trap stiffness can thus be written as

$$\kappa = 2\pi f_c \frac{k_B T}{\beta^2 D^V}. \quad (16)$$

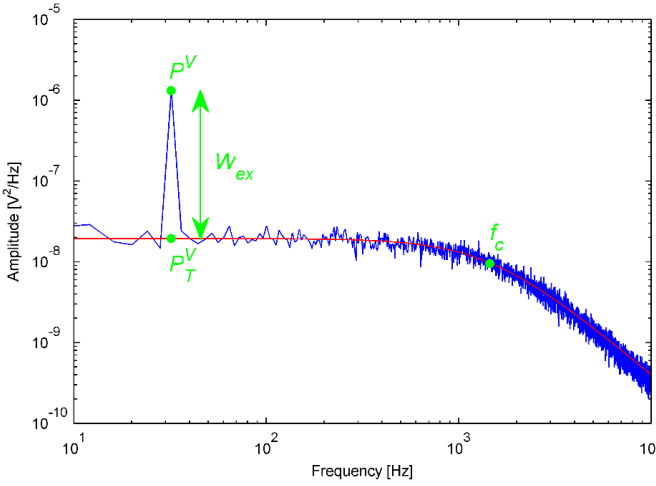


Figure 9. The power spectral density of a trapped bead with diameter of 2 μm using a laser power of 0.5 W. The red curve shows the fit to Eq. (9), where $W_{th} = 2.84 \times 10^{-15} \text{ m}^2$ and $W_{ex} = 5.26 \times 10^{-6} \text{ V}^2$ giving a β of $0.74 \times 10^{-6} \text{ m/V}$, and a corner frequency $f_c = 1453 \text{ Hz}$, yielding a trap stiffness of 172 pN/ μm .

2.3.3 Fluorescence imaging

Pili are not directly visible in bright-field microscopy since they are too small, i.e., $\sim 7 \text{ nm}$ wide and $\sim 1 \mu\text{m}$ long. To visualize surface expressed pili, as well as other functions in the cell, fluorescent tagged proteins can be used. Therefore, we incorporated a fluorescence cube with dichroic mirrors that allows transmission of the trapping laser, operating at 1064 nm along with a laser operating at 491 nm (Calypso 50, Cobolt). In front of the fluorescent laser a shutter (SH05, Thorlabs, with an apt – solenoid controller, Thorlabs)

was added. The shutter can be remotely controlled via the Hamamatsu camera software, to set the exposure times of the sample. This means that we can take fluorescence images while using the optical trap at the same time. The sample, and especially the trapped object, is strongly illuminated by the trap laser. However, since the trap laser has a wavelength of 1064 nm, the sample and the trapped object will not be immediately bleached, as is shown in Figure 10. The green arrow indicates the trapped bacteria and the red arrows indicate bacteria attached on the glass slide.

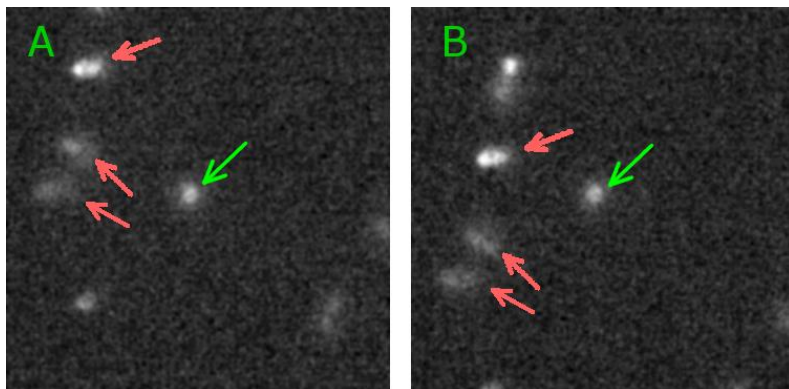


Figure 10. The fluorescent signal of a trapped bacterium (green arrow) and bacteria attached to the glass slide (red arrows). When the glass slide is moved (from panel A to panel B), the bacteria attached to the slide also move, but not the trapped bacteria.

2.3.4 Flow chamber

A force spectroscopy experiment is performed in a closed sample chamber, i.e., it is not possible to introduce and fluid flows to change the buffer or perform rolling experiments. To allow for flows, we also incorporated a flow-chamber system (Mirus Evo, Cellix) into the optical tweezers setup. The constraints were to also be able to trap and measure forces, as well as measure fluorescence simultaneously. We tested the Veno8Fluoro+ Biochips from Cellix, and found that they only produce a low auto-fluorescent signal and have a sufficiently thin bottom to allow for optical trapping, when using a water immersion objective. This setup will allow for studies such as, rolling experiments of bacteria in the presence of antibodies to see how these can prevent the adhesion of bacteria to a surface. Since it is also possible to trap particles inside the cell, it is possible to map the fluid profile accurately in

order to calculate the shear forces acting from the flowing fluid on the bacteria. A photo of the setup is given in Figure 11.

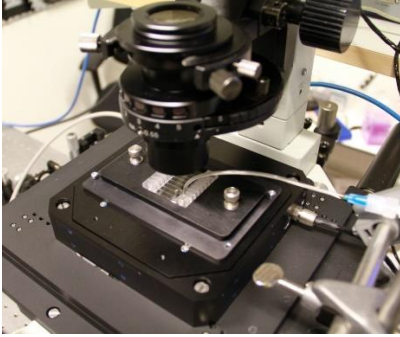


Figure 11. A picture of the flow chamber incorporated into the OT setup. To use the flow chamber, the sample holder is just replaced with a holder for the flow chamber.

3 Bacterial adhesion

Adhesion pili of uropathogenic and enterotoxigenic *E. coli* bacteria, UPEC and ETEC, respectively, facilitate adherence to host cells and are important in the first step of colonization, as well as necessary for biofilm formation [51, 52]. In addition, it has been shown that the colonization environment is related to the type of pili expressed by bacteria. For example, UPEC bacteria expressing P pili are most frequently associated with infections in the upper urinary tract, whereas bacteria expressing type 1 pili are commonly found in the lower urinary tract. On the other hand, ETEC-expressed CFA/I and CS2 pili are commonly found in the small intestine, and are associated with traveler's diarrhea [52]. Although expressed in different milieus these different pili share one structural and one mechanical feature, i.e., they are assembled into helix-like structures and can be significantly extended via uncoiling under a constant force. However, the force required to uncoil a pilus as well as their kinetic structural parameters are slightly different for pili within the same group, e.g., UPEC [11, 53–55], but significantly different when comparing groups, e.g., UPEC and ETEC expressed pili [56–58]. This interesting finding is something I have studied in my thesis and the framework for this started with the investigation of UPEC expressed P and type 1 pili.

3.1 Environmental conditions

The hydrodynamic conditions in the urinary tract create a harsh and unfriendly environment with high turbulent fluid flows in the lower urinary tract and strong vortices from the peristaltic motion in the upper urinary tract. It has been shown that the boluses that transport the urine created by the peristaltic motion can reach flow velocities up to 30 mm/s [59]. Also, the motion of the bolus will induce a complex flow field with both backflows and fluid vortices [60, 61]. In the lower part of the urethra, the flow can locally reach 10^3 mm/s during urine expel, which transforms the flow from laminar to turbulent [62, 63]. Close to the surface a thin layer (tens of microns) exists at which the flow is considered laminar even if the flow in the center is turbulent. It is known that turbulent flows give rise to so called sweeps or ejections, which can reach into the laminar viscous sublayer and thereby expose bacteria to significantly increased drag forces for ms-long periods [64, 65]. These sweeps are created by vortices outside the viscous sublayer, temporarily increasing the shear rate near the surface [66]. It is within this

harsh environment the bacteria need to first adhere to the host cell and then remain attached to start an infection.

3.2 *Pili structure and mechanics*

For the cell to remain attached in harsh environments the structures that mediate the adhesion to the surface, i.e., the pili, must be optimized in some way. A pilus is comprised by thousands of proteins (sub-units) that form a higher ordered helical polymer by non-covalent bonds between sub-units. Sub-units are connected head-to-tail, as illustrated in the uncoiled part of Figure 12, by donor strand complementation, which is significantly stronger than the layer-to-layer interactions forming the coiled part. In the coiled part subsequent turns, with ~ 3 sub-units per turn, of the polymer are stabilized via multiple interactions between residues from neighboring sub-units.

The total length of pili varies, however, they are in general $\sim 1\ \mu\text{m}$ long and 7-8 nm wide [67]. For P and type 1 pili, the shaft is comprised of ~ 4.1 and ~ 5.7 nm long, sub-units, with a molecular mass of ~ 16.5 and ~ 15.8 kDa, respectively [15, 68]. Figure 12 shows a 3D reconstruction of a P pilus. At the tip of the pilus, the adhesin that binds to receptors on host-cells is located (not shown in the figure). Under tensile stress it has been shown that the helix-like structure can be uncoiled, as illustrated in the right side of Figure 12.

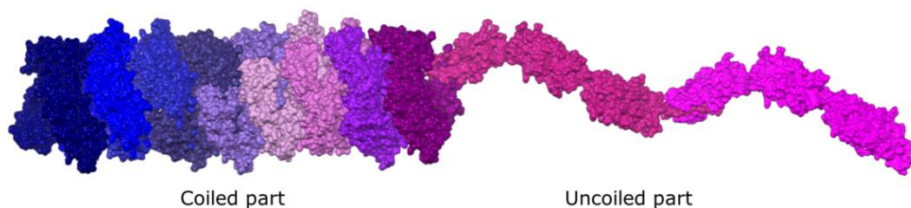


Figure 12. A high-resolution 3D reconstruction map of P pili composed of PapA sub-units. The left hand side shows the coiled part, i.e., how the pili looks when it is at rest. The right hand side show how the pilus looks like when its helical structure has been uncoiled by a tensile force.

3.2.1 Investigation of pili mechanics using OT

In order to measure the mechanical properties of pili using optical tweezers, we performed force spectroscopy measurements. Figure 13 shows an illustration of how a force spectroscopy measurement is performed and the assay used. First, large beads ($10\ \mu\text{m}$ in diameter) are immobilized to a $24 \times 60\ \text{mm}$ coverslip (no.1, Knittel Glass, Braunschweig, Germany) by drying $10\ \mu\text{l}$ of a bead-water solution for 60 min at 60°C . Thereafter, the

surface is coated by adding a solution of 20 μL of 0.01% poly-L-lysine (catalog no. P4832, Sigma-Aldrich, St. Louis, MO) to the sample, which was incubated for 45 min at 60°C . This coating will make the bacteria stick to the large beads since poly-L-lysine is positively charged and the bacteria negatively charged, respectively. Double-sticky tape was added to the coverslip to form a ~ 5 mm wide channel on the coverslip. A 20×20 mm coverslip was placed on the tape, forming a channel. This method has been proved reliable and have been used extensively [11, 56, 69, 70]. The channel is filled by putting a small drop of phosphate-buffered saline (PBS; $1 \times$, pH 7.4) solution containing 2 μm polystyrene beads and bacteria at one of the openings. The channel will fill itself by capillary forces. The openings are finally sealed with vacuum grease (Dow Corning, Midland, MI) to prevent drying of the sample.

Using the optical trap, a bacterium is thereafter mounted on the large bead by pushing the bacterium onto the large bead. A small bead is thereafter trapped and moved in vicinity of the bacterium to attach pili as described in detailed in [71]. When one or several pili are attached to the small bead, the sample is moved away from the large bead using the piezo stage, thus stretching the pilus, while the force applied to the small bead is measured. To measure recoiling force, the sample is simply moved in the opposite direction allowing the pilus to recoil.

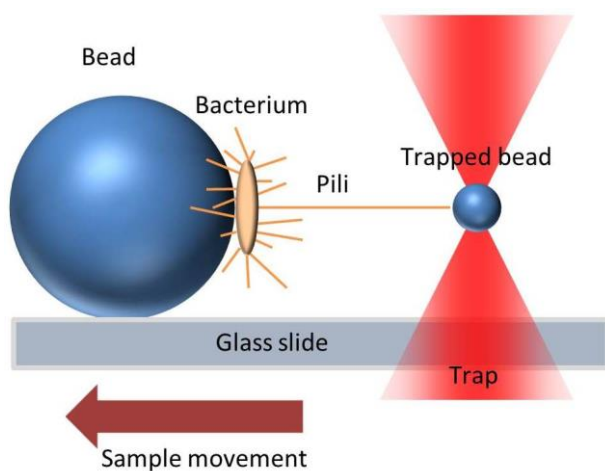


Figure 13. An illustration of how the force spectroscopy measurements are performed. The large bead is immobilized to the glass slide on which a bacterium is mounted. When the glass slide is moved, the pili will be extended.

The force response of the uncoiling of pili during such an experiment can be divided into three distinct regions; I), stretching of the layer-to-layer (*ll*) bonds, II), sequential opening of the *ll*-bonds, and III), stretching of the head-to-tail (*ht*) bonds. Figure 14 shows the results of a typical force spectroscopy measurement of a P pilus with the regions marked. The force plateau at 28 pN (defined as the steady-state force (ss-force)) is generated by the sequential opening of the sub-units in region II [72]. The constant plateau (region II) is also velocity dependent, implying that, the faster the structure is uncoiled, the higher force is required to uncoil the structure. This dynamic response can provide with information of the *ll*-bonds in the structure.

To assess these properties, i.e., the velocity dependence of the uncoiling, force-extension measurements are performed at a set of different velocities. By plotting the mean uncoiling force in region II versus the elongation velocity for each velocity, and fitting Eq. (24) to the data (see section 3.2.3 and Figure 15), properties such as the bond opening length and corner velocity (defined below) can be found. A theoretical description of the pili uncoiling mechanics is presented in following next section.

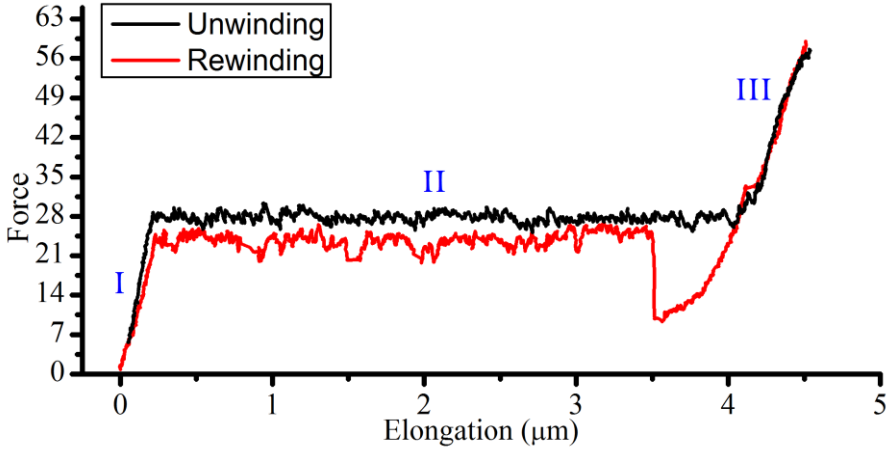


Figure 14. A typical force-extension response of a P pilus assessed by an optical tweezers force spectroscopy. The black curve represents to the uncoiling force, whereas the red curve represents the recoiling force.

After the structure has been uncoiled, and if the tensile stress is reduced, the pilus will recoil itself and return to its initial coiled state. The red curve in Figure 14 shows the recoiling force, i.e., the force the pilus is pulling with during recoiling. As can be seen, the recoiling has the same shape of the force

response as the uncoiling, except at the transition between region III and II. Here a clear “dip” can be seen. This “dip” comes from a slack in the pilus before the sub-units start to form its helical shape, i.e., there is no nucleation point for recoiling [73, 74].

3.2.2 Theoretical description of uncoiling of a helix-like pili

As is described above, the uncoiling force response can be divided into three regions. The second region is where the uncoiling, and thus the extension, of the helix-like structure occur. The uncoiling velocity is dependent on the tensile load, F , acting on the pilus. As is described in detail in refs. [75, 76], the uncoiling velocity, \dot{L} , can be expressed in terms of the difference between the uncoiling and the recoiling rates of a single layer-to-layer (ll) interaction, $k_{AB}(F)$ and $k_{BA}(F)$, multiplied with the opening length Δx_{AB} of the ll -interaction, i.e., as

$$\dot{L} = [k_{AB}(F) - k_{BA}(F)] \Delta x_{AB}, \quad (17)$$

where A and B represent the closed and open states in the energy landscape. For a conventional slip bond, the uncoiling and recoiling rates can, according to Bell [77], be expressed as

$$k_{AB}(F) = k_{AB}^{th} e^{F \Delta x_{AT} \beta_T}, \quad (18)$$

$$k_{BA}(F) = k_{AB}^{th} e^{(V_0 - F \Delta x_{TB}) \beta_T}, \quad (19)$$

where k_{AB}^{th} is the thermal opening rate of the ll -interaction, Δx_{AT} is the bond length, i.e., the distance between the ground state and the transition state T , $\beta_T = 1/k_B T$, V_0 is the energy difference between the ground and open states of the ll -interaction, and Δx_{TB} is the distance between the transition state and the open state. The uncoiling velocity, \dot{L} , can thereby be expressed in terms of the applied force F as

$$\dot{L} = \Delta x_{AB} k_{AB}^{th} \left(e^{F \Delta x_{AT} \beta_T} - e^{(V_0 - F \Delta x_{TB}) \beta_T} \right). \quad (20)$$

When the pilus is partly extended, but not subjected to any change in length the uncoiling and recoiling rates are equal, i.e., $k_{AB}(F) = k_{BA}(F)$. By equalizing Eqs. (18) and (19), we can define the steady-state force (denoted

as the ss-force)

$$F_{ss} = \frac{V_0}{\Delta x_{AB}}, \quad (21)$$

where Δx_{AB} is given by $\Delta x_{AT} + \Delta x_{TB}$. The pilus will uncoil when the tensile force is higher than the ss-force. This force is independent of the elongation velocity for velocities up to the so called corner velocity, \dot{L}^* , which is defined below.

For extension velocities above the corner velocity, or when the pilus is exposed to forces significantly larger than the steady state uncoiling force, the opening rate becomes significantly larger than the closing rate, i.e. $k_{AB}(F) \gg k_{BA}(F)$. This implies that the second term in Eq. (20) can be neglected, whereby the extension velocity can be expressed as

$$\dot{L} = \Delta x_{AB} k_{AB}^{th} e^{F \Delta x_{AT} \beta_T}. \quad (22)$$

Under these conditions, the extension velocity is exponentially dependent on the force, which, in turn, implies that the uncoiling force depends logarithmically on the uncoiling velocity. When this takes place, the extension is said to take place under dynamic conditions. The corner velocity, which is found by setting $F = F_{ss}$ in Eq. (22), is then given by

$$\dot{L}^* = \Delta x_{AB} k_{AB}^{th} e^{V_0 \Delta x_{AT} \beta_T / \Delta x_{AB}}. \quad (23)$$

The corner velocity is the velocity that separates the, steady-state and dynamic region.

Finally, by using Eqs. [(20), (21), and (23)], it is possible to express the uncoiling velocity in terms of the corner velocity and the ss-force

$$\dot{L} = \dot{L}^* e^{(F - F_{ss}) \Delta x_{AT} \beta_T} \left[1 - e^{-(F - F_{ss}) \Delta x_{AB} \beta_T} \right]. \quad (24)$$

This is thus an expression for the extension velocity that is valid under both steady-state and dynamic conditions.

3.2.3 Investigation of CS2 mechanics

CS2 pili are a type of helix-like pili expressed by ETEC bacteria, which is found on bacteria involved with diarrheal infections. We investigated the CS2

mechanics using the OT and described its mechanics using theory presented above [58]. We specifically investigated the dynamic uncoiling and recoiling mechanics of the CS2 pilus, which are vital in the adhesion process. The mean uncoiling force at different velocities is represented by the black dots in Figure 15. The blue dashed curve is a linear fit to the dynamic region using Eq. (22), i.e., where $k_{AB}(F) \gg k_{BA}(F)$. The grey dashed line is a fit to the steady-state region, Eq. (21), i.e., where $k_{AB}(F) = k_{BA}(F)$. The corner velocity is found where these two regions intersect (cyan dashed vertical line), given by Eq. (23). The red dashed curve represent the fit using the full rate equations, Eq. (24).

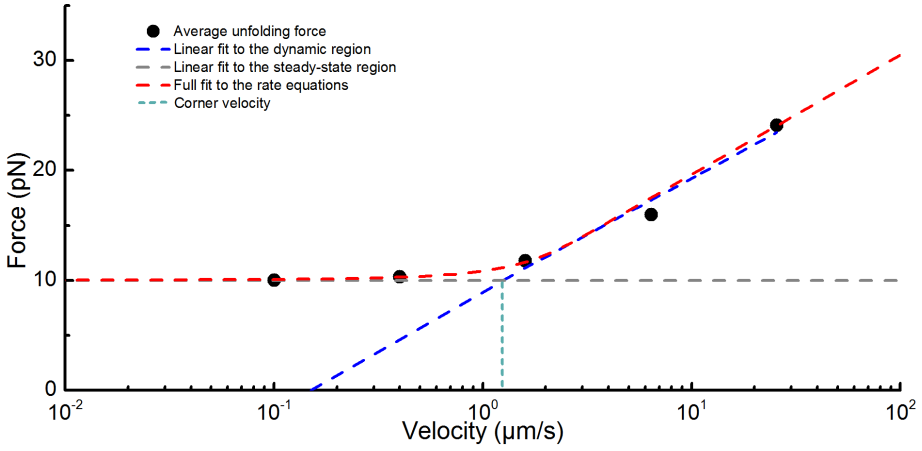


Figure 15. Force data from a dynamic force spectroscopy measurement of a CS2 fimbria at uncoiling velocities of 0.1, 0.4, 1.6, 6.4, and 25.6 mm/s sampled at 5 kHz. Each data point (black dots) shows the average uncoiling force of CS2. The blue dashed curve is a linear fit to the dynamic region, and the grey dashed curve is a linear fit to the steady-state region. The red dashed line shows a fit to the full rate equation. The corner velocity is marked with a cyan vertical dashed line.

Figure 15 shows that for low uncoiling velocities, up to the corner velocity at $\sim 1 \mu\text{m/s}$, the force response is $\sim 10 \text{ pN}$. When fitting the full rate equations Eq. (24), the best fit parameters for the experimental data were, $\Delta x_{AT} = 0.86(10) \text{ nm}$, $\Delta x_{AB} = 5.0(5) \text{ nm}$, and $\dot{L}^* = 1300(200) \text{ nm/s}$. As can be seen from the figure, the model fits the data well.

3.2.4 Simulations – Rigid body model

To get a better understanding of the uncoiling and recoiling force, i.e., the force response of helix-like pili, we constructed a physical rigid-body model based upon structural data [74]. Since both P and Type 1 pili are well characterized according to their structure, both at the sub-unit and quaternary level, we used these as model systems. All of the major pili sub-units were represented by rigid bodies, i.e., solid inelastic square rods, which were assembled using structural data. Figure 16 shows a section of a partially uncoiled rigid body model representing a P pilus (compare to Figure 12).



Figure 16. A partially uncoiled rigid body model representing a P pilus of 30 sub-units.

The simulation was performed in the same manner as the force spectroscopy experiments. The left end sub-unit was locked representing the interaction with the large bead. The force was applied on the right end sub-unit, which also was free to rotate, i.e., a virtual bead, representing the interaction with the trapped bead in an optical tweezers force spectroscopy experiment. The virtual bead was pulled to the right with a given velocity. When the pilus was fully uncoiled and stretched, the bead was moved in the opposite direction to allow the structure to recoil. The force response from one such simulation can be seen in Figure 17. As can be seen, the force response is similar to the experimental response displaced in Figure 14, and the uncoiling can be divided into the same three regions; a) The pilus initially started at rest, and when the force was applied, the *ll*-bonds started to stretch giving a linear increase in force; b) sequential uncoiling of the major pili sub-units during which the force is kept at a constant plateau, and; c) all *ll*-bonds have been opened and the *ht*-bonds is being stretched. The recoiling can be similarly divided into four regions; d) gradual shortening of the *ht*-bonds until the attraction of *ll*-bonds takes overhand; e) The slack in the recoiling force comes from the lack of nucleation points; f) Sequential recoiling of the major pili sub-units; g) the pili is fully recoiled and the *ll*-bonds was shortening until they are in rest state (same as the initial state).

Nucleation is the initial step in the formation of a structure, in this case when the first sub-units coil into the helical structure via self-assembly of the sub-units. When the first nucleation occurs, i.e., the first three sub-units coils to the helical shape, the succeeding sub-unit are pulled closer towards the already built structure. This makes it easier for the next sub-unit to also coil to the helical structure, which causes a chain-reaction that continues until there is a balance between the tension in the pilus and the mechanical load of the optical trap.

The results from this work provide further support to the previously given explanation of the force response of a helix-like pili under tensile stress [76]. These results also strengthen the hypothesis that there must be a significant slack in the pilus before the recoiling starts, causing the dip in the recoiling force response curve. Finally, the model could also mimic the influence of antibodies on P pili mechanics. The result is shown in ref. [78].

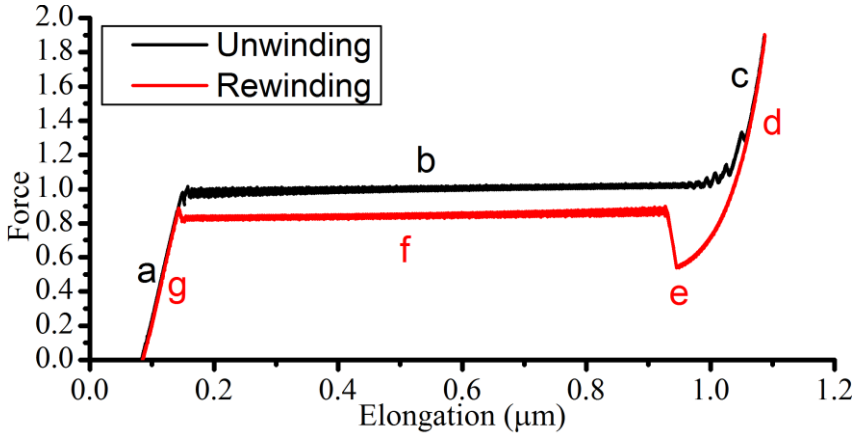


Figure 17. The normalized force extension data using the rigid body model of 250 sub-units. The indices represent different configurations of the pili: a) stretching of the *ll*-bonds, b) uncoiling of the *ll*-bonds, c) stretching of the *ht*-bonds, d) shortening of the *ht*-bonds, e) slack before the recoiling starts, f) sequential recoiling of the helix-like structure, and g) shortening of the *ll*-bonds.

3.2.5 Simulations – Pili as a shock absorber, a 1D model

To get a better understanding of how the mechanics of pili is affecting the load on the adhesin we simulated a bacterial cell (modeled as a spherical bead) attached with one pilus to a receptor in a fluid flow [79]. An illustration of the simulation setup is shown in Figure 18. The anchor point in this

simulation was a virtual attachment point for the pili and neither the anchoring point nor the pilus interacts with the surrounding fluid. Also, the sphere was assumed to be far away from any surface and placed in a uniform laminar flow. Thus, we did not simulate the spheres interaction with the surface.

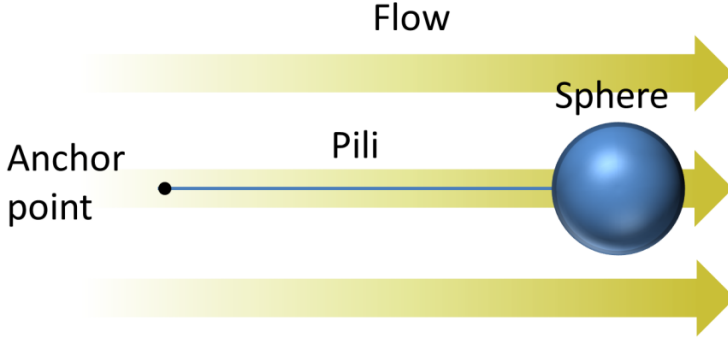


Figure 18. Illustration of the simulation setup. The sphere is representing a bacterium that is attached with a pilus to a virtual anchoring point in a laminar flow.

In a laminar flow, the force from the liquid acting on a sphere is described by the Stokes drag. For drag forces below the ss-force, the pilus will completely resist any movement of the sphere, and the force experienced by the anchoring point is described solely by Stokes drag force. However, if the drag force is higher than the ss-force, the pilus will start to uncoil the quaternary structure, allowing the sphere to “go with the flow”, thus reducing the relative velocity between the sphere (bacterial cell) and the liquid. This reduction of the velocity can be expressed by combining Stokes drag force and Eq. (24) as

$$v_{flow} = \frac{F}{6\pi\eta r} + \dot{L}^* e^{(F-F_{ss})\Delta x_{AT}\beta} \left[1 - e^{-(F-F_{ss})\Delta x_{AB}\beta} \right]. \quad (25)$$

Note that the elongation of region I (see Figure 13) is neglected in this simulation. Figure 19 presents the force experienced by the anchor point at different flow velocities when a 2 μm sphere is attached with a P and type 1 pilus, respectively. The result from this simulation shows an interesting effect of pilus uncoiling. As can be seen in Figure 19 the force experienced by the anchor point levels out at ~ 80 pN for the P pilus (red curve). This means that the pili can modulate, i.e., reduce, the force upon the cell to ~ 80 pN for a

wide range of flows, thereby working as a shock absorber for the cell. Similarly, the type 1 pili will modulate the force to ~ 125 pN (blue curve). Thus, the results from this study show that the helix-like pili can provide the bacterium with important advantages when adhering to the host cell in harsh fluidic environmental conditions.

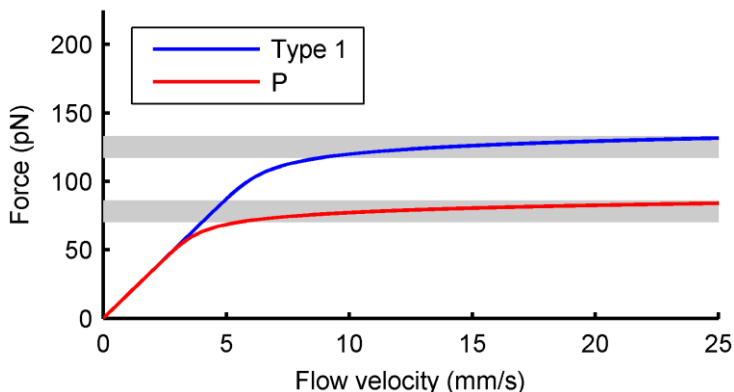


Figure 19. The modulated force response of a $1\ \mu\text{m}$ radius bead attached to a type 1 and P pili respectively. The grey horizontal lines represent the maximum experienced load on the adhesin due to the dynamic uncoiling of the helical structure of the pili.

3.2.6 Simulations – Pili as a shock absorber, a 2D model

To extend the work from 1D, we expanded the model to simulate initial attachment for a bacterium in 2D, which is more similar to the initial attachment of a bacterial cell to a host surface [80]. In Figure 20 an illustration of the model environment is presented. The flow was assumed to have the flow profile as given in Figure 20, i.e., was set to zero at the surface but increased linearly with the height above the surface. The initial position of the bacterium was directly above the anchoring point and the initial velocity of the bead was given the same as the flow velocity at the initial height. When the simulation was started, the bacterium moved towards the surface where the trajectory depended on the mechanical properties of the pilus. As an example, for a stiff pilus, the trajectory will follow that of the dashed arrow, while if it can be extended and the shear force is high enough to uncoil the structure, it will follow a trajectory similar to the grey solid arrows.

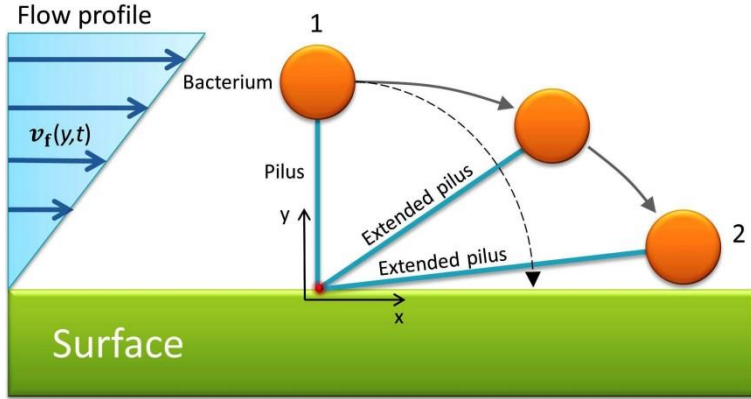


Figure 20. The trajectory of a bacterium tethered to a surface with a stiff linker (black dashed arrow) and an extendable pilus that elongates by uncoiling when the shear force is higher than the uncoiling force (grey solid arrows).

The trajectory of the sphere and the force experienced by the anchoring point (representing the adhesin) is presented in Figure 21 for two cases; a stiff linker and a type 1 pilus. The shear rate was set to 5400 s^{-1} , corresponding to a flow velocity of 16 mm/s at $3 \text{ }\mu\text{m}$ above the surface, which is reasonable for a sweep in the lower urethra [65]. The trajectory of the sphere is shown in Figure 21A for the stiff linker (black solid curve) and the type 1 pilus (blue dashed curve), respectively. Here, the type 1 pilus was uncoiled due to the shear rate reducing the load on the adhesin. As can be seen in Figure 21B, the force experienced by the adhesin for the stiff linker was $\sim 225 \text{ pN}$, and for the type 1 pilus, $\sim 125 \text{ pN}$. Again, this shows how pili uncoiling can provide the bacteria with an advantage during initial attachment and continued adhesion to the host cell under harsh hydrodynamic conditions.

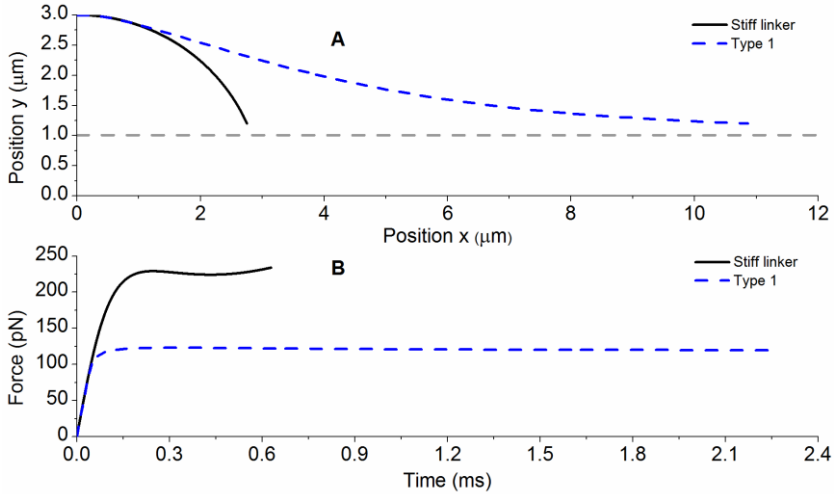


Figure 21. (A) Trajectory of a bacterium tethered with either a stiff linker (solid black curve) or a type 1 pilus (blue dashed curve). The bacterium modeled has an effective radius of $1.0\ \mu\text{m}$ and the length of the tether is $2\ \mu\text{m}$. The position given represents the center position of the bacterium. The gray dashed horizontal line therefore represents the position at which the bacterium touches the surface. (B) The force experienced by the adhesin in the various cases.

3.3 Modeling the adhesion

The adhesin, the protein that binds to receptors on the host cell, is a vital part of the function of pili since the bacteria are mediating attachment via this structure. Generally, there are two types of adhesins modeled, either a slip bond or catch-bond [81, 82]. A slip bond can be modeled as if the lifetime of the bond decreases exponentially with mechanical load as illustrated by the red-dashed curve in Figure 22. In contrast, the catch-bond can be modelled having three states; a weak state, a strong state, and an unbound state. At low mechanical load, the bond will reside in the weak state, where the bond lifetime is low, implying that the adhesin-receptor complex will break easily. However, if the load is increased the bond will go through a conformational change implying an increased bond lifetime as illustrated by the blue curve. It is assumed that these mechanical properties give the catch-bond an advantage over the slip bond since it gives the bacteria the possibility to spread under low shear, and stay firmly attached during high shear rates [83].

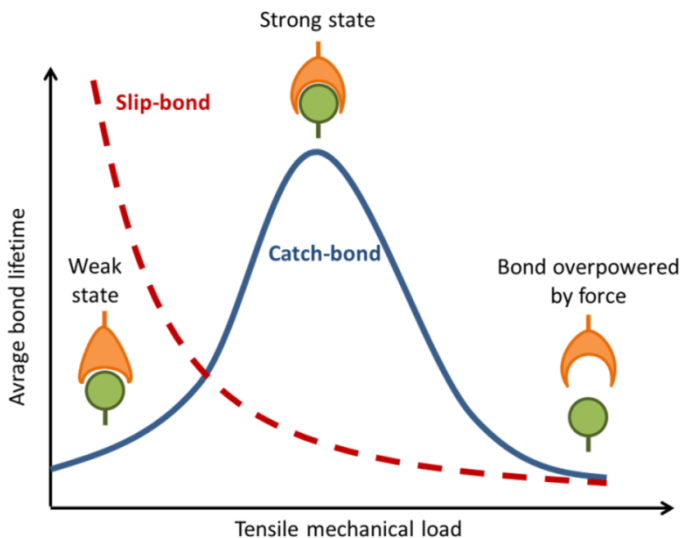


Figure 22. Illustration of the mechanical function of the slip and catch-bond. The slip-bond lifetime gets shorter with increasing load while the catch-bond can undergo a conformational change to increase its lifetime when the load is increased.

3.3.1 Catch-bond mechanics

The survival of the bond anchoring the pilus to the host is crucial for a bacterium to cause an infection. Therefore, the adhesin has been thoroughly investigated, especially by the research group of Wendy Thomas et al [82]. They investigated the mechanical properties of the FimH-mannose bond expressed at the tip of the type 1 pilus. They found that this adhesin-receptor behaves as a catch-bond and that bacteria manage to adhere better when the shear force was above a certain threshold level. The catch-bond can switch between three different states; a weak, a strong, and an unbound state, depending on the mechanical load and loading rate.

They further designed a theoretical model describing the complex mechanical function of the catch-bond. This model can explain and predict *E. coli* bacteria rolling on mannose-BSA and force spectroscopy data performed by constant-velocity AFM experiments [82, 84]. They described the mechanics of catch-bond by two differential equations containing the transition rates between each of the three states. Each equation describes the change in probability of being in state i , where $i=1$ represents the weak state and state $i=2$ represents the strong state. The probability the FimH-mannose bond to be in respective state as a function of time is thus described by

$$\frac{dB_1(t)}{dt} = -\{k_{10}[F(t)] + k_{12}[F(t)]\}B_1(t) + k_{21}[F(t)]B_2(t), \quad (26)$$

and

$$\frac{dB_2(t)}{dt} = k_{12}[F(t)]B_1(t) - \{k_{20}[F(t)] + k_{21}[F(t)]\}B_2(t), \quad (27)$$

where k_{10} , k_{20} , k_{12} , and k_{21} represent the transition rate coefficients for transitions from state 1 to state 0 (off state), from state 2 to state 0, from state 1 to state 2, and from state 2 to state 1 [82]. These have an exponential dependence on the force, described by the Bell equation, $k_{ij}[F(t)] = k_{ij}^0 \exp[F(t) \cdot x_{ij} / k_B T]$, where k_{ij}^0 is the thermal rate constant, where i , and j represents the three aforementioned states. $F(t)$ represents the time dependent applied force, and x_{ij} is the distance to the transition state [77]. The rate constants and distance parameters are given in Table 1 below.

Table 1. Parameters used in the FimH allosteric catch-bond model taken from Ref [84].

Transition	Rate constant (s ⁻¹)	Distance parameter (Å)
1 → off	$k_{10}^0 = 1.37$	$x_{10} = 2.85$
2 → off	$k_{20}^0 = 5.1 \cdot 10^{-6}$	$x_{20} = 4.52$
1 → 2	$k_{12}^0 = 3.3 \cdot 10^{-5}$	$x_{12} = 15.1$
2 → 1	$k_{21}^0 = 0.11$	$x_{21} = -3.88$

3.3.2 Simulations – survival probability

The uncoiling of a pilus and bacterial trajectory will also affect the survival probability of the FimH adhesin. The results in section 3.2.6 describe how the force acting on the adhesin-receptor bond is affected by the mechanical properties of the pilus and the fluid conditions. To get a better understanding of how these forces affect the lifetime of the adhesin-receptor bond, and thereby the bacterial adhesion lifetime, the 2D model described in section 3.2.6 was extended to also include the catch-bond properties of the FimH adhesin. The survival probability for the two cases discussed in section 3.2.6, i.e., a stiff linker and a type 1 pilus, is presented in Figure 23. As can be seen,

the survival probability for the case with a type 1 pilus remains close to 1 at all times whereas for the stiff linker rapidly goes towards zero. In the inset, a small drop before the plateau can be seen. This drop originates from the transition from state 1 to state 0, before the force becomes large enough to make the transition from state 1 to state 2, after which the plateau is seen.

By comparing the survival probability with the stiff linker and type 1 pilus, it is clear that the uncoiling mechanics of the helix-like pili is greatly beneficial for the bacterium. These results thus further support that the uncoiling mechanics is a vital function for the bacterial adhesion.

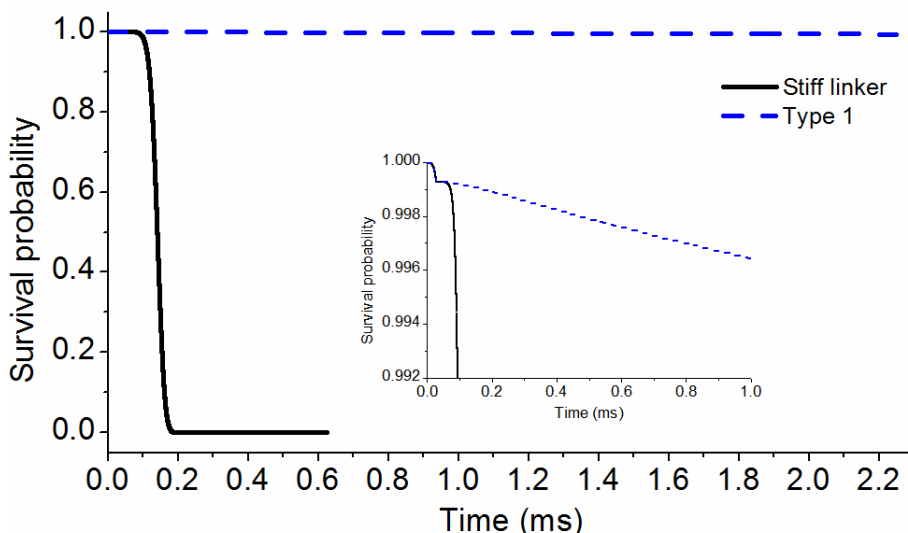


Figure 23. Survival probability for a FimH-mannose bond when the bacterium is tethered via a stiff linker (solid curve) or a type 1 pilus (blue dashed curve). The figure shows that for the stiff linker, the survival probability rapidly decreases toward zero in <0.2 ms, whereas for the type 1 pilus it remains close to 1. Inset) The plateau represents the period after the catch-bond changes conformation state from the weak to the strong binding configuration.

3.4 Corrections to Stokes' drag force

Cell adhesion under hydrodynamic conditions near a surface involves complex interactions that can be both difficult to model and time consuming to simulate. To reduce the complexity of the system and to decrease computational time, various types of approximations are often used. In particular, force simulations of tethered particles in viscous sub-layers are

often uncritically performed by the use of the Stokes' drag force without taking into account surface correction coefficients and force components such as lift, buoyancy, added mass, the Basset force, and the finite inertia of the cell. It is not at all obvious that all these can be neglected when tethered cells attached to a surface are considered; on the contrary, it is most plausible that several of these can modify the force a cell experiences in a given shear flow.

A lot of work has been done investigating how these corrections, combined with Stokes drag force, compare to the Navier-Stokes equations (NSE). The NSE is a set of time-dependent nonlinear partial differential equations that describe the flow of fluids. The validity of the approach of adding terms to Stokes' drag force has been verified numerous times [85–95]. For motion close to a surface the Basset force model used in this work was not modified to take into account surface effects since it is difficult to handle numerically. This slightly overestimates the drag force for objects in proximity of the surface, as discussed in refs. [92, 94], but do not significantly change the outcome of the analysis.

To describe the force on an object arising from a fluid in a laminar flow (i.e., Reynolds number, $Re < 1$), Stokes drag force can be used. Since tethered bacteria are close to the surface, they will be situated in a viscous sub-layer in which the flow acts laminar. The thickness of this sub-layer in a pipe is described by ref. [96], pages 290-295. As an example, assuming a diameter of 5 mm, and a maximum flow velocity of 1 m/s (in the urethra during urine expel), Re is ~ 5000 giving a thickness of the viscous sub-layer of $\sim 150 \mu\text{m}$. Since we investigate initial attachment, the bacteria will be significantly closer than $150 \mu\text{m}$ validates the use of Stokes drag force even if the flow higher up is turbulent.

To investigate the effect of aforementioned corrections, we simulated the movement of a tethered sphere in a fluid flow with a given shear rate [97], see Figure 24 for illustration of the simulation setup. Using this setup, the equation of motion can simply be expressed as

$$m \frac{\partial v_{bx}}{\partial t} = F_{Fx}(t) - F_{Tx}(t), \quad (28)$$

$$m \frac{\partial v_{by}}{\partial t} = F_{Fy}(t) - F_{Ty}(t), \quad (29)$$

where m is the mass of the cell and $F_{Fi}(t)$ and $F_{Ti}(t)$ are the fluid and

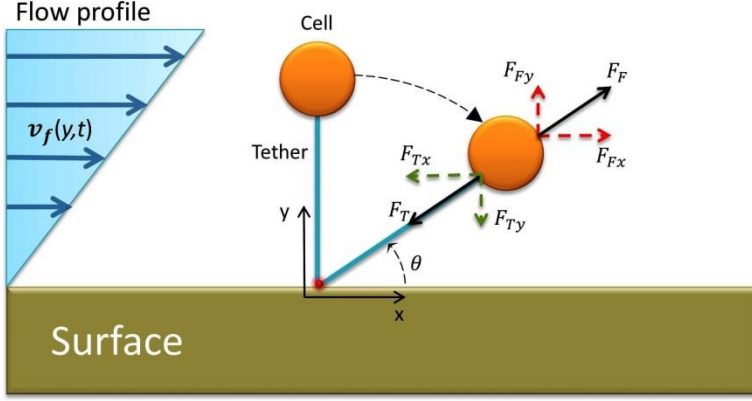


Figure 24. The simulation setup with force components on the tether and from the flow indicated by the red and green dashed arrows.

tether force components, and v_{bi} is the cell velocity (where i represents x - or y -direction). The force from the fluid was assumed to have contributions from the drag force in the proximity of a surface, $\mathbf{F}_D(t)$, a lift force, $\mathbf{F}_L(t)$, a buoyancy force, $\mathbf{F}_B(t)$, the Basset force, $\mathbf{F}_{BF}(t)$, and from the added mass, $\mathbf{F}_A(t)$, giving

$$\mathbf{F}_F(t) = \mathbf{F}_D(t) + \mathbf{F}_L(t) + \mathbf{F}_B(t) + \mathbf{F}_{BF}(t) + \mathbf{F}_A(t). \quad (30)$$

These force components are further described below.

3.4.1 Stoke drag force – Near surface correction

The fluid drag on a sphere is often modeled by the Stokes' drag force. However, although commonly used, this expression is valid only for particles in free flow, i.e., far from any surface. Since the cells considered in this work are tethered close to a surface, the Stokes' drag force has to be modified to account for the presence of the surface. This can be done by so-called near surface correction coefficients. Since the corrections are dissimilar in the parallel and the normal directions to the surface, the two force components are given by

$$F_{Di}(t) = C_i 6\pi\eta r [v_{fi}(t) - v_{bi}(t)], \quad (31)$$

where i represents x - and y - direction, C_i is the surface correction coefficient, v_{fi} is the flow velocity in direction i , and v_{bi} is the particle velocity in direction i .

For a sphere moving parallel to a surface in a shearing flow Goldman et al. [98] presented a correction to the Stokes drag force model valid for large distances from the surface. Later, an interpolation formula was derived by Chaoui and Feuillebois [99], which is also valid close to the surface, given by

$$C_x[y(t)] = \sum_{i=0}^N c_i h^{-i}(t), \quad (32)$$

where N is the polynomial order, c_i are coefficients that all are given reference [99], and h is the normalized wall distance given by $h = y(t)/r$. This interpolation is valid at any distance from the surface.

For a sphere moving perpendicular to the surface, Schäffer et al. [100] derived an interpolation formula

$$C_y[y(t)] = \left\{ 1 - \frac{9}{8}h^{-1} + \frac{1}{2}h^{-3} - \frac{57}{100}h^{-4} + \frac{1}{5}h^{-5} + \frac{7}{200}h^{-11} - \frac{1}{25}h^{-12} \right\}^{-1}, \quad (33)$$

which for $r/y > 1.1$ deviates less than 0.1% from the exact result by Brenner [101].

3.4.2 Added mass

When an object is accelerated it has to displace/accelerate the surrounding media. The additional force required to do this is called the added mass, and is given by

$$m_A = \frac{2}{3}\pi r^3 \rho_f, \quad (34)$$

where ρ_f is the density of the surrounding media [102]. This means that the effective mass of the sphere is the sum of the true particle mass and the added mass.

3.4.3 Basset force

The acceleration and deceleration of a body in a fluid will experience a history force called the Basset force. This history force results from the effect of a lagging boundary layer development due to a change in relative velocity, and can be expressed as

$$\mathbf{F}_{BF} = -6\pi\eta r^2 \frac{1}{\sqrt{\pi\nu}} \int_0^t \frac{d[v_{fi}(t) - v_{bi}(t)]}{d\tau} \frac{d\tau}{\sqrt{t-\tau}}, \quad (35)$$

where ν is the kinematic viscosity, and t is the accumulated time from the start of the simulation [89].

3.4.4 Lift force

When a sphere rotates or moves parallel to a surface in a shear flow, the sphere will experience a force perpendicular to the flow, called the lift force. The lift produced by a sphere was investigated by Saffman [103]. However, this is not valid close to any surface. A model for the lift force for non-rotating sphere near a surface was later developed by Cherukat and McLaughlin [104], and is given by

$$\mathbf{F}_L(t) = F_L(t)\hat{\mathbf{y}} = \rho_f \left[v_{fi}(t) - v_{bi}(t) \right]^2 r^2 L(t)\hat{\mathbf{y}}, \quad (36)$$

where $L(t)$ is a parameterized function which is described in detail in ref. [104].

3.4.5 Buoyancy

Buoyancy is an upward force exerted by a fluid on an immersed object. The net buoyancy can be expressed in terms of the difference in density between the sphere and the surrounding media, i.e., as

$$\mathbf{F}_B(t) = F_B(t)\hat{\mathbf{y}} = (\rho_f - \rho_s)Vg\hat{\mathbf{y}}, \quad (37)$$

where ρ_s is the density of the sphere, V is the volume of the sphere, and g is the gravitational constant.

3.4.6 Results and conclusions

To investigate the influence of the surface correction coefficients, C_x and C_y , and the additional force components; lift, buoyancy, the Basset force, finite inertia, and added mass on the force response at the anchoring point of a tether, simulations were performed for cells attached by a stiff linker for a wide range of shear rates (10 to 10^4 s^{-1}) and cell sizes (radius of 1 to $5 \text{ }\mu\text{m}$). The tether length was set to two times the diameter of the cell. For each shear rate and size configuration, a set of simulations were performed; one

simulation with all terms included, and a set of simulations where one of the components were excluded in each simulation.

The relative force contributions is defined as $(F' - F)/F'$, where F' and F are the forces of a full simulation and a simulation with one force component excluded, respectively, evaluated at the peak force of the full simulation. The simulations showed that the surface correction coefficients are at all cases important. The parallel surface correction contributed with 5-8% and the normal surface correction contributed with 23-27%. These corrections are, however, developed under steady-flow conditions but were used as an ad hoc approximation, which is supported by the results in ref [92].

The lift force and the inertia contribute with less than 1% in all cases and can thereby be considered insignificant in these types of simulations. For the lowest shear rate, 10 s^{-1} , the buoyancy force contributes with only ~2 % to the total force, and can thereby for higher shear rates and smaller radii be considered insignificant (the density of the cell was set 7% higher than the surrounding liquid. The Basset force contributes with up to 19% for the highest shear rate and largest bead. One should note that the Basset force model used in this work is not modified to take into account surface effects since it is difficult to handle numerically. This slightly overestimates the drag force for objects in proximity of the surface, as discussed in refs. [92, 94], but do not change the outcome of the analysis. In conclusion, this work shows that it is often crucial to include appropriate approximations to Stokes drag force, like the basset force and the near surface corrections, when simulating tethered particles near a surface. Lift and inertia are important only at high shear rates, and buoyancy are important in low shear rates.

4 Method to detect expression of surface organelles

The pili expressed by, e.g., UPEC bacteria are too thin and narrow to visualize in conventional bright-field microscopes, although it would be very beneficial to know whether a cell is expressing pili or not prior to force spectroscopy measurements. Therefore we developed a fast and simple method to detect the presence of pili on a single cell while working with the sample. The method is based on comparing the effective-diameter, experimentally measured using the “oscillation method” described in section 2.3.2, and an analytical model of the cell using a bright-field image of the cells projected area.

To describe the drag force of a non-spherical object, Leith modified the Stokes drag force to include a shape factor [105],

$$F_D = 3\pi\mu V d_c K, \quad (38)$$

where V is the velocity of the sphere, d_c the cross section diameter, and K is the dynamic shape factor. Together d_c and K represent the effective diameter ($d_{Mod} = d_c K$) of the cell and the dynamic shape factor is given by

$$K = \frac{1}{3} + \frac{2}{3} \frac{d_s}{d_c}, \quad (39)$$

where $d_c = 2\sqrt{A_{cross}/\pi}$ and $d_s = \sqrt{A_{surf}/\pi}$, where A_{cross} is the cross section area and A_{surf} is the projected area of the object.

To test the method, we used well defined silica microspheres coated with a polymer brush and *E. coli* bacteria with different degrees of piliation. A bacterium was modeled as a cylinder with spherical caps. To find the projected area, A_{cross} , a bright-field image was taken of the object to find the dimensions, as seen in Figure 25A. The projected area is given by $A_{cross} = \pi d^2/4 + d(L-d)$, where L is the length and d is the width of the bacterium. This will give the effective diameter of a sphere representing the bacterium as

$$d_{Mod} = \frac{2}{3\sqrt{\pi}} \sqrt{\frac{\pi d^2}{4} + d(L-d)} + \frac{2}{3} \sqrt{dL}. \quad (40)$$

When imaging a cell in bright-field mode the pili cannot be detected implying that the maximum projected area, or effective diameter, is directly given by the outer cell membrane. This is illustrated in Figure 25A.

The diameter of the object is in turn assessed experimentally using the optical tweezers, as illustrated in Figure 25B-C. By oscillating the object, the effective diameter of the sphere representing the trapped object is given by

$$d_{Exp} = \frac{k_B T}{3\pi\eta\beta^2 D^V}. \quad (41)$$

Since any pili expressed by a cell will interact with the fluid a higher drag, i.e., larger effective diameter, is measured than what the expected from the image.

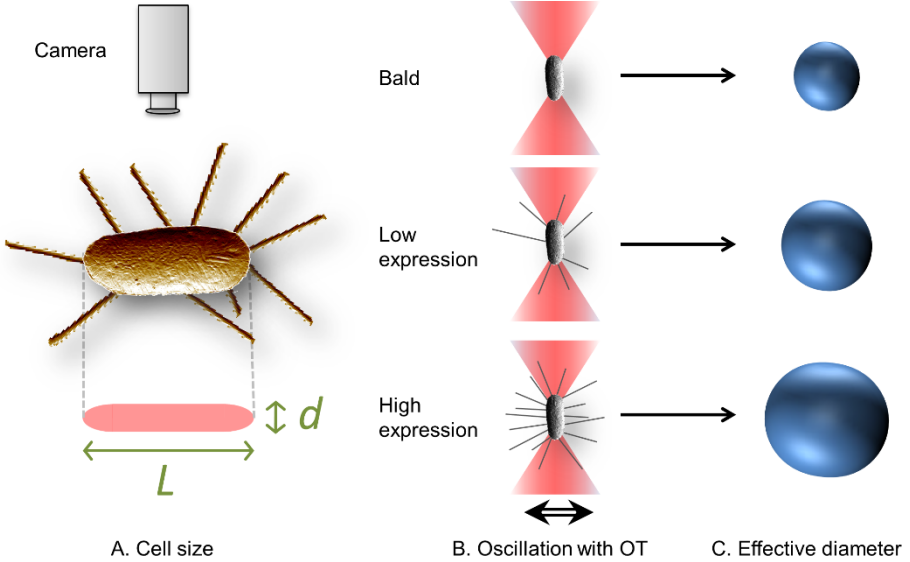


Figure 25. A) Bright-field image of the cell from which its dimensions was measured, in which the surface organelles cannot be seen. B) The model-effective diameter was calculated from the image. C-D) the object was oscillated, from which the experimental-effective diameter could be calculated.

To verify the model, we used *E. coli* bacteria expressing; no pili, P pili, and type 1 pili, respectively. To find whether the bacteria are expressing pili,

the experimental and model-effective diameters are compared. If the experimental diameter is significantly larger than the modeled, the cell expresses some surface organelles not seen in the bright-field. The effective diameters from the three sets of experiments are presented in Figure 26. The black line have a slope of 1, and corresponds to a perfect match between the model-effective diameter and the experimental-effective diameter. And as can be seen, for the bald cells, respective diameter (blue circles) are close to the black line, representing a good match between the model and experiment, and thereby verifying the model. The experimental-effective diameter is much higher for the piliated cells compared to the expected model-effective diameter. This indicates that the cells express pili.

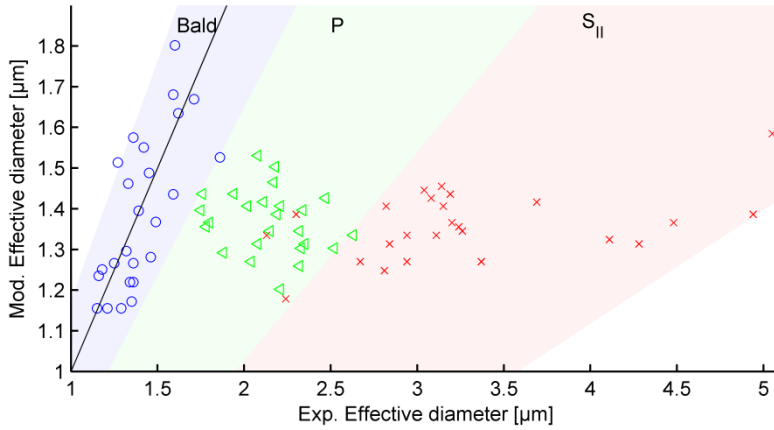


Figure 26. The model-effective diameter versus the experimental-effective diameter using the optical tweezers. For the bald bacteria (blue circles), the model and experimental diameter are very similar as expected. The green triangles and red crosses represent the effective diameter for P pili and S_{II} pili respectively.

5 Digital Holographic Microscopy

Digital holography microscopy (DHM) is a technique using 2D-Fourier transforms to reconstruct the phase and amplitude of a propagating light field from a hologram image. A hologram image is an image of the diffraction pattern of an object taken behind the object when it is illuminated by light from a coherent light source, i.e., laser or LED. We implemented the DHM in our existing OT setup, as illustrated in Figure 27, as a first step to develop a technique to identify bacteria and the height at which they move in a flow chamber. This technique can also be used for non-invasively measuring the flow profile in, e.g., a flow chamber by high-speed imaging of holograms from beads.

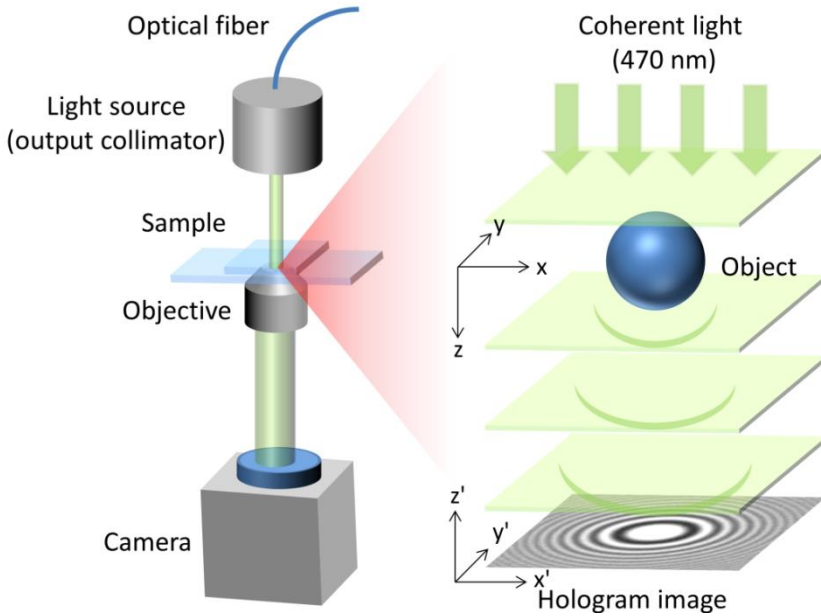


Figure 27. An illustration of the experimental setup is shown to the left whereas a zoom-in of a spherical object, illuminated with a coherent light source, is shown to the right with a resultant hologram image. The origins for the x, y, z and x', y', z' coordinate systems were positioned at the center of the object and at the center of the hologram plane, respectively.

DHM is a powerful technique and from a single hologram image, it is possible to assess parameters such as thickness, volume, and the refractive index of both living as well as dead cells [106, 107]. Also, the axial position of the object, relative to the hologram can be reconstructed [108, 109]. We

therefore evaluated the technique and possibility to assess morphological changes in cells and the axial position of the cells [110].

To investigate if it is possible to assess morphological changes in cells, we used the original in-line version of holography, referred to as Gabor holography, which can shortly be explained as follows [111]. Consider a small semi-transparent particle illuminated by a plane wave. The particle will scatter a fraction of the incident light field, and due to the interferences of the scattered and non-scattered fields, the irradiance, I , recorded on the detector (i.e., the hologram) can be given by

$$I = |U_O + U_R|^2 = |U_O|^2 + |U_R|^2 + U_O U_R^* + U_O^* U_R, \quad (42)$$

where U_O and U_R are the scattered and the non-scattered (reference) amplitude, respectively, and $*$ denotes a complex conjugate. The scattered amplitude is normally much smaller than the amplitude of the reference, implying that the first term of Eq. (42) is negligible. By convolution, the reconstructed amplitude (in the x', y', z' coordinate system) can be given by

$$U(x', y', z') = \mathbf{F}^{-1} \left[\mathbf{F} \{ U(x, y) \} \cdot \mathbf{F} \{ h(x' - x, y' - y; z') \} \right], \quad (43)$$

where h is the complex impulse response function

$$h = \frac{z' e^{jkr}}{j\lambda r^2}, \quad (44)$$

where z' is the axial distance from the hologram plane (image plane) to the reconstruction plane, k is the wave number, j is the complex number, and the distance r is given by $r = \sqrt{z'^2 + (x' - x)^2 + (y' - y)^2}$ where x, y , and x', y' are the lateral co-ordinates at the hologram and reconstruction planes, respectively. By numerically solving Eq. (43), the intensity profile along the optical axis can be evaluated, and its focus, which is used for position detection, can be found.

The setup was built around an Olympus IX 71 microscope, normally used for OT force spectroscopy measurements, which was modified to illuminate the sample according to an in-line holography setup. The light source (a collimated low-cost LED, operating at 470 nm (M470L3-C1, Thorlabs)) was collimated using a free space collimator consisting of a microscope objective (Plan N 10x/0.25, Olympus) mounted on a fiber

holder (MBT613, Thorlabs). The objective focused the light from the LED into a multi-mode (MM) fiber (QMMJ-3AF3AF-IRVIS-50/125-3-5, OZ Optics) and an output collimator (HPUFO-2, A3A-400/700-P-17-180-10AC, OZ Optics) was mounted just above the piezo-controlled microscope stage holding the sample (PI-P5613CD, Physik Instruments). The MM fiber allowed for frequency filtering of the light and for easy and stable arrangement of the illumination source.

A set of hologram images were acquired, starting from 30 μm behind the object (9.685 μm polystyrene bead (4210A, Thermo Scientific)) with 10 μm steps to 100 μm behind the object. The reconstructed position of the geometrical focus versus the actual position of the bead can be found in Figure 28. The red squares represent the reconstruction of the holograms simulated using Zemax, where the same environmental conditions as in the experiments were used. The green squares correspond to the reconstruction of the experimental holograms. As can be seen, the reconstruction can

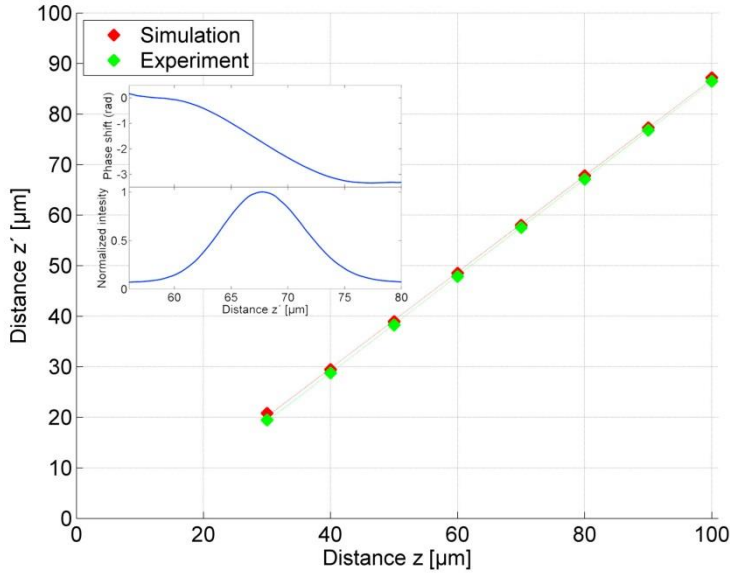


Figure 28. Piezo-position vs. reconstructed position of the focus. Red squares represent the reconstructed positions of the simulation and the red line is a linear fit to the data. Similarly, the green squares represent the experimental data with the corresponding linear fit. The inset shows the Gouy phase shift and intensity around the reconstructed focus for the image acquired at 80 μm behind the object in the simulation.

perfectly predict the position both of the simulated and experimental data. The top panel in the inset in Figure 28 shows the Gouy phase shift of $\sim\pi$ over the focus [112], and the lower panel shows the intensity along the optical axis (for the hologram at 80 μm).

To investigate if it is possible to determine morphological changes on a complex shape, we turned to the red blood cell (RBC). We immobilized RBCs on a glass slide in a Phosphate Buffered Saline (PBS) solution keeping them in their natural shape. Hologram images were thereafter taken at distances from 30 to 100 μm (with fixed steps of 10 μm). The hologram images were reconstructed, where the position the geometrical focus versus the actual position of the RBC is plotted with green dots in Figure 29A. To compare with the experiment, we simulated a RBC using a Cassini shaped model [113], with parameter values of, $a = 2.2$, $b = 2.25$, and $c = 0.66$ μm representing a 6.3 μm wide RBC-like object with an homogenous index of refraction of 1.40 [114]. The Cassini model was imported into Zemax and illuminated in a similar manner as the experiments. The reconstructed geometrical focus of the simulated hologram images is plotted with red dots in Figure 29A.

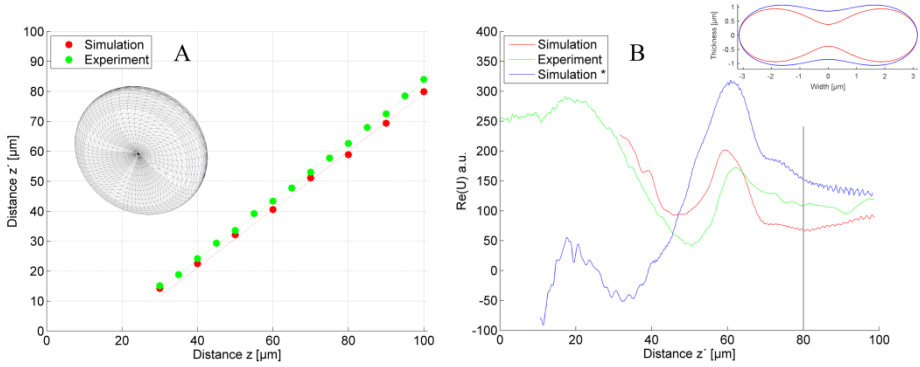


Figure 29. A) The reconstructed distance to the focus of the simulated RBC (red) and the experiment using a real RBC (green). The inset shows the Cassini model of the RBC used in the simulations. B) The reconstructed $\text{abs}(U) \cdot \cos(\theta_R - \theta)$ for the simulated unaltered RBC and a deformed RBC represented by the red and blue curves, respectively and for the experiment using a real RBC (green). The grey vertical line indicates the position of the RBC.

In addition to the analysis of the intensity distribution we investigated the back-reconstructed profile of $\text{abs}(U) \cdot \cos(\theta_R - \theta)$, where θ_R and θ is the phase of the reference field and the reconstructed field respectively, i.e.,

$\theta_R - \theta$ is the phase shift due to the refraction of the field. The results for the RBC and simulated RBC are presented in Figure 29B, with the green and red curves, respectively. As can be seen, the red and green curves agree well between 30 and 70 μm , particularly the dip at ~ 50 μm and the peak at ~ 60 μm . We also investigated how a small morphological change of the RBC affected the $\text{abs}(U) \cdot \cos(\theta_R - \theta)$. The parameters of the Cassini model were changed to $a = 2.1$, $b = 2.35$, and $c = 0.66$ μm making the RBC slightly deformed, see the inset in Figure 29B for a cross-section profile. The $\text{abs}(U) \cdot \cos(\theta_R - \theta)$ of the deformed RBC changed in comparison to the unaltered RBC, see the blue curve in Figure 29B. In particular, the peak at ~ 60 μm is larger and the dip at 50 μm is shifted to ~ 35 μm as well as lowered. This means that a small change in the shape of the object gives rise to a big shift in the profile. These results show that this method accurately can reconstruct the position of small objects, both spherical and non-spherical. In addition, this method can detect small morphological changes in living cells such as red blood cells.

6 Summary of appended papers and my contributions

Paper I

Biomechanical and structural Features of CS2 Fimbriae of Enterotoxigenic Escherichia coli

In this work, the mechanical property of the CS2 pili, expressed by enterotoxigenic *Escherichia coli* (ETEC) bacteria, was investigated. The steady-state uncoiling force and bond kinetics were assessed and compared to other ETEC expressed pili, which showed a strong correlation. Homology modeling was also performed of the major structural sub-unit (CotA) revealing the hydrophobicity and charge of the sub-unit.

My contribution: In this work, I designed the new optical system used for trapping and I wrote the calibration and measurement program used for force spectroscopy measurements. I also wrote the theory regarding the uncoiling mechanics of the pili and helped with the analysis of the force spectroscopy data.

Paper II

Rigid multibody simulation of a helix-like structure: the dynamics of bacterial adhesion pili

We developed a rigid multi-body model of a helix-like polymer to get a better understanding of its uncoiling and recoiling response. A pilus was modelled by using rigid bodies' that were assembled according to structural data. The simulation showed good agreement, both for uncoiling and recoiling, with experimental results for type 1 and P pili. The model could also account for antibodies binding to the surface of the pilus, whose results were also in consistence with experimental data. Thus, the model and the results from this work gave an enhanced understanding of pili mechanics.

My contribution: I contributed to all parts of the work. My main task was to revise and improve the model that previously had been developed in a master thesis project. I also added the possibility to simulate the effect of antibodies binding to the pilus, did the analysis, made the majority of the figures, and wrote parts of the manuscript.

Paper III

Helix-like biopolymers can act as dampers of force for bacteria in flows

Pili are crucial in bacterial attachment. The function and purpose of some specific mechanical functions of the pili are yet not fully investigated. In this work, we showed that the uncoiling of these helix-like pili can reduce the force experienced by the adhesin-receptor interaction at the tip of each individual pilus. The results indicate that for moderate flows (~ 25 mm/s); the pilus can reduce the load on the adhesin by a factor of ~ 6 and ~ 4 , for P and type 1 pili respective, by uncoiling its helical structure. This means that this type of pili can act as a force damper for the adhesin.

My contribution: I contributed to all parts of the work. I wrote the code and did the simulations, the analysis, the majority of the figures, and wrote parts of the manuscript.

Paper IV

The shaft of the Type 1 Fimbriae Regulates an External Force to Match the FimH Catch bond

It is assumed that the type 1 pili and the FimH-mannose adhesin have co-evolved to optimize binding to the host cell. In this work, we developed a model that describes the force experienced by the adhesin, and how it is modeled by the type 1 pili. The model also solves the motion of the bacterium when it moves towards the surface. It is found that the experienced force is limited to ~ 120 pN, even at high shear rates due to pili uncoiling. This force is sufficient to make the conformational change in the adhesin to the strong state, but not too strong so the bond immediately breaks. This supports our assumption that the adhesion and pili are optimized for each other.

My contribution: I contributed to all parts of the work. I wrote the code and did the simulations, the analysis, the figures, and wrote parts of the manuscript.

Paper V

Tethered cells in fluid flows – beyond the Stokes' drag force approach

Simulations of tethered cells near a surface are usually performed solely using Stokes' drag force, which might not be accurate in all cases. In this work, we investigated the effect of surface corrections, lift forces, buoyancy, the Basset force, the cells' finite inertia, and added mass. We show that the force at the anchor point is significantly underestimated ($\sim 32 - 46\%$) if none of the aforementioned terms are included, showing the importance of including important corrections.

My contribution: I contributed to all parts of the work. I wrote the code and did the simulations, part of the theoretical work, the analysis, the figures, and wrote parts of the manuscript.

Paper VI

Detecting the presence of surface organelles at the single cell level, a novel cell sorting approach

Surface structures like pili are important for cell adhesion, but they cannot be seen in conventional bright-field microscopes since they are too small. In this work, we developed a method that can detect the presence of surface organelles using optical tweezers. This is done by first taking a bright-field image of the object and using theoretical model calculating the model-effective diameter of the sphere representing the object. Then, by oscillating the object in the optical trap, an experimental-effective diameter of the sphere representing the trapped object can be found. By comparing these two diameters, we can determine if the object are expressing any surface organelles.

My contribution: I contributed to most parts of the work. I did the single cell experiments and the analysis, did most of the figures, and wrote parts of the manuscript.

Paper VII

Cell shape identification using digital holographic microscopy

The distance to the image plane of small unfocused objects and morphological changes of cells cannot be detected in conventional bright-field microscopy. In this work, we presented a simple and fast digital holographic microscopy method for identification of position and geometrical shapes of cells. We tested the method using holograms generated in a ray-tracing software and hologram images from experiments with semitransparent beads and red blood cells. We showed that using the back-reconstructed intensity and phase, the method can provide information about the geometrical shape and the position of the object. The method can thus be used to measure morphological changes in cells.

My contribution: I contributed to all parts of the work. I refined a previous developed code and did a major part of the simulations. I performed the experiments, the analysis, made the figures, and wrote parts of the manuscript.

7 Acknowledgements

Magnus Andersson – for being a great supervisor, always pointing me in the right direction, and for motivating me to start biking again.

Krister Wiklund – for helping and teaching me with fluid dynamics and all discussions about training.

Ove Axner – for being a great teacher, both during my undergraduate and graduate studies, always with a sense of humor.

Narges Mortezaei – for being a great colleague, officemate, and friend.

Pontus Svenmarker – for helping me in the lab and being a good friend.

Bhupender Singh – for being a great officemate and teaching me cell biology.

Staffan Schedin – being a fruitful collaborator and introducing me to holography

Daniel Vågberg – for helping me with C-programming and being a good friend.

Jörgen Eriksson – for always being happy to help with whenever was needed.

Katarina, Ann-Charlott, Lilian, Gabriella, and Carina – for all help with the administrative stuff.

Martin Stefan – for being a good friend and guiding me in the jungle of bikes and skies.

Isak Silander – for being a good friend and helping me with electronics.

Daniel Zakrisson – for helping me with Fourier optics and being an adventurer always up for new expeditions and fika.

Lena Åström and Peter Wikström – For helping me with stuff in the workshop.

The physics staff – Robin Sandström, Hanqing Zhang, Thomas Hausmaninger, Nils Blix, Patrik Nordqvist, Tiva Sharif, Patrik Stenmark, Alexandra Johansson, Jens Zamanian, Petter Lundberg, Martin Servin, Jenny Enevold, Mattias Lindh, Thomas Lanz, Maria Hamrin, Sune Pettersson, Roushdey Salh, Petter Holme, Peter Olsson, Nicolas Boulanger, Michael Bradley, and all the others in the department of physics.

Mats Nylén and Vitaly Bychkov – you will be remembered.

Family, relatives and friends

8 References

1. Steffen, R.: Epidemiology of Traveler's Diarrhea. *Clin. Infect. Dis.* 41, 536–540 (2005).
2. DuPont, H.L.: Systematic review: the epidemiology and clinical features of travellers' diarrhoea. *Aliment. Pharmacol. Ther.* 30, 187–196 (2009).
3. World Health Organization: Future directions for research on enterotoxigenic *Escherichia coli* vaccines for developing countries. *Wkly. Epidemiol. Rec.* 97–104 (2006).
4. Roos, V., Ulett, G.: The asymptomatic bacteriuria *Escherichia coli* strain 83972 outcompetes uropathogenic *E. coli* strains in human urine. *Infect. Immun.* 74, 615–624 (2006).
5. Stamm, W.E., Norrby, S.R.: Urinary tract infections: disease panorama and challenges. *J. Infect. Dis.* 183 Suppl, S1–S4 (2001).
6. McDonnell, G., Russell, a. D.: Antiseptics and disinfectants: Activity, action, and resistance. *Clin. Microbiol. Rev.* 12, 147–179 (1999).
7. Donnenberg, M.S.: Pathogenic strategies of enteric bacteria. *Nature.* 406, 768–774 (2000).
8. Soto, G.E., Hultgren, S.J.: Bacterial Adhesins : Common Themes and Variations in Architecture and Assembly. 181, 1059–1071 (1999).
9. Sauer, F.G., Mulvey, M.A., Shilling, J.D., Martinez, J.J., Hultgren, S.J.: Bacterial pili : molecular mechanisms of pathogenesis. *Curr. Opin. Microbiol.* 65–72 (2000).
10. Sussman, M., Gally, D.L.: The biology of cystitis: host and bacterial factors. *Annu. Rev. Med.* 50, 149–158 (1999).
11. Andersson, M., Uhlin, B.E., Fällman, E.: The biomechanical properties of *E. coli* pili for urinary tract attachment reflect the host environment. *Biophys. J.* 93, 3008–14 (2007).
12. Li, Y.-F., Poole, S., Nishio, K., Jang, K., Rasulova, F., McVeigh, A., Savarino, S.J., Xia, D., Bullitt, E.: Structure of CFA/I fimbriae from enterotoxigenic *Escherichia coli*. *Proc. Natl. Acad. Sci. U. S. A.* 106, 10793–8 (2009).
13. Verger, D., Bullitt, E., Hultgren, S.J., Waksman, G.: Crystal structure of the P pilus rod subunit PapA. *PLoS Pathog.* 3, e73 (2007).

-
14. Bullitt, E., Makowski, L.: Structural polymorphism of bacterial adhesion pili. *Nature*. 373, 164–167 (1995).
 15. Bullitt, E., Makowski, L.: Bacterial adhesion pili are heterologous assemblies of similar subunits. *Biophys. J.* 74, 623–32 (1998).
 16. Whitfield, M., Ghose, T., Thomas, W.: Shear-stabilized rolling behavior of *E. coli* examined with simulations. *Biophys. J.* 99, 2470–2478 (2010).
 17. Thomas, W.E., Nilsson, L.M., Forero, M., Sokurenko, E. V, Vogel, V.: Shear-dependent “stick-and-roll” adhesion of type 1 fimbriated *Escherichia coli*. *Mol. Microbiol.* 53, 1545–57 (2004).
 18. Fällman, E., Schedin, S., Jass, J., Uhlin, B.E., Axner, O.: The unfolding of the P pili quaternary structure by stretching is reversible, not plastic. *EMBO Rep.* 6, 52–6 (2005).
 19. Ashkin, a: Acceleration and Trapping of Particles by Radiation Pressure. *Phys. Rev. Lett.* 24–27 (1970).
 20. Ashkin, a., Dziedzic, J.M.: Optical levitation by radiation pressure. *Appl. Phys. Lett.* 19, 283–285 (1971).
 21. Ashkin, a: Applications of laser radiation pressure. *Science*. 210, 1081–1088 (1980).
 22. Ashkin, a, Dziedzic, J.M., Bjorkholm, J.E., Chu, S.: Observation of a single-beam gradient force optical trap for dielectric particles. *Opt. Lett.* 11, 288–290 (1986).
 23. Ashkin, a, Dziedzic, J.M.: Optical trapping and manipulation of viruses and bacteria. *Science*. 235, 1517–1520 (1987).
 24. Rohrbach, A.: Switching and measuring a force of 25 femtoNewtons with an optical trap. *Opt. Express*. 13, 9695–9701 (2005).
 25. Neuman, K.C., Nagy, A.: Single-molecule force spectroscopy: optical tweezers, magnetic tweezers and atomic force microscopy. *Nat. Methods*. 5, 491–505 (2008).
 26. Dholakia, K., Čižmár, T.: Shaping the future of manipulation. *Nat. Photonics*. 5, 335–342 (2011).
 27. Seeger, S., Monajembashi, S., Hutter, K.J., Fütterman, G., Wolfrum, J., Greulich, K.O.: Application of laser optical tweezers in immunology and molecular genetics. *Cytometry*. 12, 497–504 (1991).
-

-
28. Ashkin, a., Dziedzic, J.M., Yamane, T.: Optical trapping and manipulation of single cells using infrared laser beams. *Nature*. 330, 769–771 (1987).
 29. Ayano, S., Wakamoto, Y., Yamashita, S., Yasuda, K.: Quantitative measurement of damage caused by 1064-nm wavelength optical trapping of *Escherichia coli* cells using on-chip single cell cultivation system. *Biochem. Biophys. Res. Commun.* 350, 678–684 (2006).
 30. Neuman, K.C., Chadd, E.H., Liou, G.F., Bergman, K., Block, S.M.: Characterization of photodamage to *Escherichia coli* in optical traps. *Biophys. J.* 77, 2856–2863 (1999).
 31. Mirsaidov, U., Timp, W., Timp, K., Mir, M., Matsudaira, P., Timp, G.: Optimal optical trap for bacterial viability. *Phys. Rev. E - Stat. Nonlinear, Soft Matter Phys.* 78, 1–7 (2008).
 32. Rasmussen, M.B., Oddershede, L.B., Siegmundfeldt, H.: Optical tweezers cause physiological damage to *Escherichia coli* and *Listeria* bacteria. *Appl. Environ. Microbiol.* 74, 2441–2446 (2008).
 33. Andersson, M., Fällman, E., Uhlin, B.E., Axner, O.: Force measuring optical tweezers system for long time measurements of P pili stability. *Proc. SPIE.* 6088, 286–295 (2006).
 34. Fällman, E., Schedin, S., Jass, J., Andersson, M., Uhlin, B.E., Axner, O.: Optical tweezers based force measurement system for quantitating binding interactions: system design and application for the study of bacterial adhesion. *Biosens. Bioelectron.* 19, 1429–1437 (2004).
 35. Magazzú, a., Spadaro, D., Donato, M.G., Sayed, R., Messina, E., D’Andrea, C., Foti, a., Fazio, B., Iatí, M. a., Irrera, a., Saija, R., Gucciardi, P.G., Maragó, O.M.: Optical tweezers: a non-destructive tool for soft and biomaterial investigations. *Rend. Lincei.* (2015).
 36. Fazal, F.M., Block, S.M.: Optical tweezers study life under tension, (2011).
 37. Thomas, N., Thornhill, R. a: The physics of biological molecular motors. *J. Phys. D. Appl. Phys.* 31, 253–266 (1999).
 38. Clemen, A.E.-M., Vilfan, M., Jaud, J., Zhang, J., Bärmann, M., Rief, M.: Force-dependent stepping kinetics of myosin-V. *Biophys. J.* 88, 4402–4410 (2005).
 39. Ling, L., Zhou, F., Huang, L., Li, Z.-Y.: Optical forces on arbitrary shaped particles in optical tweezers. *J. Appl. Phys.* 108, 073110 (2010).
-

-
40. Harada, Y., Asakura, T.: Radiation forces on a dielectric sphere in the Rayleigh scattering regime. *Opt. Commun.* 124, 529–541 (1996).
 41. Ashkin, a: Forces of a single-beam gradient laser trap on a dielectric sphere in the ray optics regime. *Methods Cell Biol.* 55, 1–27 (1998).
 42. Svoboda, K., Block, S.M.: Biological applications of optical forces. *Annu. Rev. Biophys. Biomol. Struct.* 23, 247–285 (1994).
 43. Peterman, E.J.G., Gittes, F., Schmidt, C.F.: Laser-induced heating in optical traps. *Biophys. J.* 84, 1308–1316 (2003).
 44. Neuman, K.C., Block, S.M.: Optical trapping. *Rev. Sci. Instrum.* 75, 2787–2809 (2004).
 45. Jun, Y., Tripathy, S.K., Narayanareddy, B.R.J., Mattson-hoss, M.K., Gross, S.P.: Calibration of Optical Tweezers for In Vivo Force Measurements : How do Different Approaches Compare ? *Biophysj.* 107, 1474–1484 (2014).
 46. Li, T., Raizen, M.G.: Brownian motion at short time scales. *Ann. Phys.* 525, 281–295 (2013).
 47. Capitanio, M., Romano, G., Ballerini, R., Giuntini, M., Pavone, F.S., Dunlap, D., Finzi, L.: Calibration of optical tweezers with differential interference contrast signals. *Rev. Sci. Instrum.* 73, 1687 (2002).
 48. Gittes, F., Schmidt, C.F.: Signals and noise in micromechanical measurements. *Methods Cell Biol.* 55, 129–156 (1998).
 49. Reif, F.: Fundamentals of statistical and thermal physics. McGraw-Hill Book compny, Tokyo (1965).
 50. Tolić-Nofrelykke, S.F., Schäffer, E., Howard, J., Pavone, F.S., Jülicher, F., Flyvbjerg, H.: Calibration of optical tweezers with positional detection in the back focal plane. *Rev. Sci. Instrum.* 77, 103101 (2006).
 51. Melican, K., Sandoval, R.M., Kader, A., Josefsson, L., Tanner, G. a, Molitoris, B. a, Richter-Dahlfors, A.: Uropathogenic Escherichia coli P and Type 1 fimbriae act in synergy in a living host to facilitate renal colonization leading to nephron obstruction. *PLoS Pathog.* 7, e1001298 (2011).
 52. Tchesnokova, V., McVeigh, A.L., Kidd, B., Yakovenko, O., Thomas, W.E., Sokurenko, E. V, Savarino, S.J.: Shear-enhanced binding of intestinal colonization factor antigen I of enterotoxigenic Escherichia coli. *Mol. Microbiol.* 76, 489–502 (2010).
-

-
53. Andersson, M., Axner, O., Almqvist, F., Uhlin, B.E., Fällman, E.: Physical properties of biopolymers assessed by optical tweezers: analysis of folding and refolding of bacterial pili. *ChemPhysChem*. 9, 221–35 (2008).
 54. Castelain, M., Sjöström, A.E., Fällman, E., Uhlin, B.E., Andersson, M.: Unfolding and refolding properties of S pili on extraintestinal pathogenic *Escherichia coli*. *Eur. Biophys. J.* 39, 1105–1115 (2009).
 55. Castelain, M., Ehlers, S., Klinth, J., Lindberg, S., Andersson, M., Uhlin, B.E., Axner, O.: Fast uncoiling kinetics of F1C pili expressed by uropathogenic *Escherichia coli* are revealed on a single pilus level using force-measuring optical tweezers. *Eur. Biophys. J.* 40, 305–16 (2011).
 56. Andersson, M., Björnham, O., Svantesson, M., Badahdah, A., Uhlin, B.E., Bullitt, E.: A structural basis for sustained bacterial adhesion: biomechanical properties of CFA/I pili. *J. Mol. Biol.* 415, 918–28 (2012).
 57. Mortezaei, N., Epler, C.R., P., S.P., Shirdel, M., Singh, B., McVeigh, A., Uhlin, B.E., Savarino, S.J., Andersson, M., Bullitt, E.: Structure and function of Enterotoxigenic *Escherichia coli* fimbriae from differing assembly pathways. *Mol. Microbiol.* 95, 116–126 (2015).
 58. Mortezaei, N., Singh, B., Zakrisson, J., Bullitt, E., Andersson, M.: Biomechanical and Structural Features of CS2 Fimbriae of Enterotoxigenic *Escherichia coli*. *Biophys. J.* 109, 49–56 (2015).
 59. Kinn, a C.: Progress in urodynamic research on the upper urinary tract: implications for practical urology. *Urol. Res.* 24, 1–7 (1996).
 60. Jeffrey, B., Udaykumar, H.S., Schulze, K.S.: Flow fields generated by peristaltic reflex in isolated guinea pig ileum: impact of contraction depth and shoulders. *Am. J. Physiol. Gastrointest. Liver Physiol.* 285, 907–18 (2003).
 61. Vahidi, B., Fatouraei, N., Imanparast, A., Moghadam, A.N.: A mathematical simulation of the ureter: effects of the model parameters on ureteral pressure/flow relations. *J. Biomech. Eng.* 133, 031004–1 – 031004–9 (2011).
 62. Jin, Q., Zhang, X., Li, X., Wang, J.: Dynamics analysis of bladder-urethra system based on CFD. *Front. Mech. Eng. China.* 5, 336–340 (2010).
 63. Abrams, P.: *Urodynamics*. Springer Verlag, London (1997).
-

-
64. Smith, C.R., Walker, J.D. a., Haidari, a. H., Sobrun, U.: On the Dynamics of Near-Wall Turbulence. *Philos. Trans. R. Soc. A* 336, 131–175 (1991).
 65. Xu, C., Zhang, Z., den Toonder, J.M.J., Nieuwstadt, F.T.M.: Origin of high kurtosis levels in the viscous sublayer. Direct numerical simulation and experiment. *Phys. Fluids* 8, 1938–1944 (1996).
 66. Marchioli, C., Soldati, A.: Mechanisms for particle transfer and segregation in a turbulent boundary layer. *J. Fluid Mech.* 468, 283–315 (2002).
 67. Hahn, E., Wild, P., Hermanns, U., Sebbel, P., Glockshuber, R., Häner, M., Taschner, N., Burkhard, P., Aebi, U., Müller, S. a.: Exploring the 3D Molecular Architecture of *Escherichia coli* Type 1 Pili. *J. Mol. Biol.* 323, 845–857 (2002).
 68. Forero, M., Yakovenko, O., Sokurenko, E. V., Thomas, W.E., Vogel, V.: Uncoiling mechanics of *Escherichia coli* type I fimbriae are optimized for catch bonds. *PLoS Biol.* 4, e298 (2006).
 69. Norregaard, K., Andersson, M., Nielsen, P.E., Brown, S., Oddershede, L.B.: Tethered particle analysis of supercoiled circular DNA using peptide nucleic acid handles. *Nat. Protoc.* 9, 2206–2223 (2014).
 70. Norregaard, K., Andersson, M., Sneppen, K., Nielsen, P.E., Brown, S., Oddershede, L.B.: DNA supercoiling enhances cooperativity and efficiency of an epigenetic switch. *Proc. Natl. Acad. Sci. U. S. A.* 110, 17386–17391 (2013).
 71. Axner, O., Andersson, M., Björnham, O., Castelain, M., Klinth, J., Koutris, E., Schedin, S.: Assessing bacterial adhesion on an individual adhesin and single pili level using optical tweezers. *Adv. Exp. Med. Biol.* 715, 301–313 (2011).
 72. Andersson, M., Fällman, E., Uhlin, B.E., Axner, O.: A sticky chain model of the elongation and unfolding of *Escherichia coli* P pili under stress. *Biophys. J.* 90, 1521–34 (2006).
 73. Björnham, O., Axner, O., Andersson, M.: Modeling of the elongation and retraction of *Escherichia coli* P pili under strain by Monte Carlo simulations. *Eur. Biophys. J.* 37, 381–391 (2008).
 74. Zakrisson, J., Wiklund, K., Servin, M., Axner, O., Lacoursière, C., Andersson, M.: Rigid multibody simulation of a helix-like structure: the dynamics of bacterial adhesion pili. *Eur. Biophys. J.* 44, 294–300 (2015).
-

-
75. Andersson, M., Fällman, E., Uhlin, B.E., Axner, O.: Dynamic force spectroscopy of *E. coli* P pili. *Biophys. J.* 91, 2717–25 (2006).
 76. Axner, O., Björnham, O., Castelain, M., Koutris, E., Schedin, S., Fällman, E., Andersson, M.: Unraveling the Secrets of Bacterial Adhesion Organelles using Single Molecule Force Spectroscopy. In: Gräslund, A., Rigler, R., and Widengren, J. (eds.) *Springer series in chemical physics: single molecule spectroscopy in chemistry, physics and biology*. pp. 337–362. Springer Berlin Heidelberg, Berlin, Heidelberg (2010).
 77. Bell, G.: Models for the Specific adhesion of cells to cells.pdf. *Science* (80-.). 200, 618–627 (1978).
 78. Mortezaei, N., Singh, B., Bullitt, E., Uhlin, B.E., Andersson, M.: P-fimbriae in the presence of anti-PapA antibodies: new insight of antibodies action against pathogens. *Sci. Rep.* 3, 3393 (2013).
 79. Zakrisson, J., Wiklund, K., Axner, O., Andersson, M.: Helix-like biopolymers can act as dampers of force for bacteria in flows. *Eur. Biophys. J.* 41, 551–60 (2012).
 80. Zakrisson, J., Wiklund, K., Axner, O., Andersson, M.: The shaft of the type 1 fimbriae regulates an external force to match the FimH catch bond. *Biophys. J.* 104, 2137–48 (2013).
 81. Björnham, O., Nilsson, H., Andersson, M., Schedin, S.: Physical properties of the specific PapG-galabiose binding in *E. coli* P pili-mediated adhesion. *Eur. Biophys. J.* 38, 245–54 (2009).
 82. Thomas, W.E., Forero, M., Yakovenko, O., Nilsson, L.M., Vicini, P., Sokurenko, E., Vogel, V.: Catch-bond model derived from allostery explains force-activated bacterial adhesion. *Biophys. J.* 90, 753–64 (2006).
 83. Thomas, W.E., Trintchina, E., Forero, M., Vogel, V., Sokurenko, E. V: Bacterial adhesion to target cells enhanced by shear force. *Cell.* 109, 913–23 (2002).
 84. Yakovenko, O., Sharma, S., Forero, M., Tchesnokova, V., Aprikian, P., Kidd, B., Mach, A., Vogel, V., Sokurenko, E., Thomas, W.E.: FimH forms catch bonds that are enhanced by mechanical force due to allosteric regulation. *J. Biol. Chem.* 283, 11596–605 (2008).
 85. Takemura, F., Magnaudet, J.: The transverse force on clean and contaminated bubbles rising near a vertical wall at moderate Reynolds number. *J. Fluid Mech.* 495, 235–253 (2003).
-

-
86. Zeng, L., Balachandar, S., Fischer, P.: Wall-induced forces on a rigid sphere at finite Reynolds number. *J. Fluid Mech.* 536, 1–25 (2005).
 87. Derksen, J.J., Larsen, R.A.: Drag and lift forces on random assemblies of wall-attached spheres in low-Reynolds-number shear flow. *J. Fluid Mech.* 673, 548–573 (2011).
 88. Krishnan, G., Leighton, D.: Inertial lift on a moving sphere in contact with a plane wall in a shear flow. *Phys. Fluids*. 7, 2538 (1995).
 89. Yang, F.: Interaction Law for a Collision Between Two Solid Particles in a Viscous Liquid, (2006).
 90. Ryu, S., Matsudaira, P.: Unsteady Motion, Finite Reynolds Numbers, and Wall Effect on Vorticella convallaria Contribute Contraction Force Greater than the Stokes Drag. *Biophysj.* 98, 2574–2581 (2010).
 91. Takemura, F., Takagi, S., Magnaudet, J., Matsumoto, Y.: Drag and lift forces on a bubble rising near a vertical wall in a viscous liquid. *J. Fluid Mech.* 461, 277–300 (2002).
 92. Wakiya, S.: Effect of a Plane Wall on the Impulse Motion of a Sphere in a Viscous Fluid. *J. Phys. Soc. Japan*. 19, 1401–1408 (1964).
 93. Maxey, M.R., Riley, J.J.: Equation of motion for a small rigid sphere in a nonuniform flow. *Phys. Fluids*. 26, 883–889 (1983).
 94. Felderhof, B.U.: Effect of the wall on the velocity autocorrelation function and long-time tail of Brownian motion. *J. Phys. Chem. B*. 109, 21406–21412 (2005).
 95. Franosch, T., Jeney, S.: Persistent correlation of constrained colloidal motion. *Phys. Rev. E - Stat. Nonlinear, Soft Matter Phys.* 79, 1–11 (2009).
 96. Pope, S.B.: *Turbulent Flows*. Cambridge University Press (2000).
 97. Zakrisson, J., Wiklund, K., Axner, O., Andersson, M.: Tethered cells in fluid flows—beyond the Stokes’ drag force approach. *Phys. Biol.* 12, 056006 (2015).
 98. Goldman, A., Cox, R.G., Brenner, H.: Slow Viscous Motion of a Sphere Parallel to a Plane Wall - II Couette flow, *Chem. Chem. Eng. Sci.* 22, 653–660 (1967).
 99. Chaoui, M., Feuillebois, F.: Creeping flow around a sphere in a shear flow close to a wall. *Q. J. Mech. Appl. Math.* 56, 381–410 (2003).
-

-
100. Schäffer, E., Nørrelykke, S.F., Howard, J.: Surface forces and drag coefficients of microspheres near a plane surface measured with optical tweezers. *Langmuir*. 23, 3654–65 (2007).
 101. Brenner, H.: The slow motion of a sphere through a viscous fluid towards a plane surface. *Chem. Eng. Sci.* 16, 242–251 (1961).
 102. Lamb, H.: *Hydrodynamics*. New York. Dover publications (1945).
 103. Saffman, P.G.: The lift on a small sphere in a slow shear flow. *J. Fluid Mech.* 22, 385–400 (1965).
 104. Cherukat, P., McLaughlin, J.B.: The inertial lift on a rigid sphere in a linear shear-flow field near a flat wall. *J. Fluid Mech.* 263, 1–18 (1994).
 105. Leith, D.: Drag on Nonspherical Objects. *Aerosol Sci. Technol.* 6, 153–161 (1987).
 106. Alm, K., Cirenajwis, H., Gisselsson, L., Wingren, A.G., Janicke, B., Mölder, A., Oredsson, S., Persson, J.: Digital Holography and Cell Studies. *Hologr. Res. Technol.* 237–252 (2011).
 107. Rappaz, B., Marquet, P., Cuche, E., Emery, Y., Depeursinge, C., Magistretti, P.: Measurement of the integral refractive index and dynamic cell morphometry of living cells with digital holographic microscopy. *Opt. Express*. 13, 9361–9373 (2005).
 108. Wilson, L., Zhang, R.: 3D Localization of weak scatterers in Rayleigh-Sommerfeld back-propagation. 20, 1177–1179 (2012).
 109. Lee, S.-H., Roichman, Y., Yi, G.-R., Kim, S.-H., Yang, S.-M., van Blaaderen, A., van Oostrum, P., Grier, D.G.: Characterizing and tracking single colloidal particles with video holographic microscopy. *Opt. Express*. 15, 18275–18282 (2007).
 110. Zakrisson, J., Schedin, S., Andersson, M.: Cell shape identification using digital holographic microscopy. 54, 7442–7448 (2015).
 111. Goodman, J.W.: *Introduction to Fourier Optics* 3rd Ed. Roberts & Company (2005).
 112. Visser, T.D., Wolf, E.: The origin of the Gouy phase anomaly and its generalization to astigmatic wavefields. *Opt. Commun.* 283, 3371–3375 (2010).
 113. Wriedt, T., Hellmers, J., Eremina, E., Schuh, R.: Light scattering by single erythrocyte: Comparison of different methods. *J. Quant. Spectrosc. Radiat. Transf.* 100, 444–456 (2006).
-

-
114. Wang, S., Xue, L., Lai, J., Li, Z.: Three-dimensional refractive index reconstruction of red blood cells with one-dimensional moving based on local plane wave approximation. *J. Opt.* 14, 065301 (2012).